JGR Oceans

RESEARCH ARTICLE
10.1029/2025JC023042

A Numerical 3D-2D Coupling Strategy for Simulating Landslide-Generated Tsunamis in Complex Geometries: The Taan Fiord, Alaska, Case Study

A. Romano[1,2], C. Cecioni[1], G. Bellotti[1], G. Barajas[2], and J. L. Lara[2]

[1]Department of Civil, Computer Science and Aeronautical Technologies Engineering, Roma Tre University, Rome, Italy, [2]IHCantabria—Instituto de Hidráulica Ambiental de la Universidad de Cantabria, Santander, Spain

Key Points:

- A coupling strategy between 3D and 2D models to simulate landslide-generated tsunamis in complex geometries is presented
- The method is used to simulate the 2015 Taan Fiord (AK) landslide-tsunami event, a complex and well-documented case with field data
- A sensitivity analysis, by varying the position of the coupling boundary, is performed to provide practical guidance for coupling methods

Supporting Information:

Supporting Information may be found in the online version of this article.

Correspondence to:

A. Romano,
alessandro.romano@uniroma3.it

Citation:

Romano, A., Cecioni, C., Bellotti, G., Barajas, G., & Lara, J. L. (2025). A numerical 3D-2D coupling strategy for simulating landslide-generated tsunamis in complex geometries: The Taan Fiord, Alaska, case study. *Journal of Geophysical Research: Oceans*, *130*, e2025JC023042. https://doi.org/10.1029/2025JC023042

Received 20 JUN 2025
Accepted 5 NOV 2025

Author Contributions:

Conceptualization: A. Romano, C. Cecioni, G. Bellotti, J. L. Lara
Data curation: A. Romano, C. Cecioni
Formal analysis: A. Romano, C. Cecioni, G. Bellotti, G. Barajas
Funding acquisition: G. Bellotti
Investigation: A. Romano, C. Cecioni, G. Bellotti, G. Barajas, J. L. Lara
Methodology: A. Romano, C. Cecioni, G. Bellotti, J. L. Lara
Software: A. Romano, C. Cecioni, G. Barajas
Supervision: J. L. Lara
Validation: A. Romano, C. Cecioni, G. Barajas
Visualization: A. Romano, C. Cecioni

Abstract Landslide-generated tsunamis represent a significant hazard, specifically in coastal, fjord, and lake environments. The accurate modeling of these complicated phenomena is crucial for risk assessment and preparation of mitigation strategies. Landslide-generated tsunamis can be modeled using either three-dimensional (3D) computational fluid dynamics or depth-integrated two-dimensional (2D) numerical models. 3D models are valuable for the modeling in the near-field, however their computational cost is often prohibitive for simulating long-range wave propagation (far-field). 2D models are very efficient for simulating tsunami propagation over large areas, but cannot capture the full complexity of the generation process. In this paper, we propose a coupling strategy between 3D and 2D models for simulating tsunamis induced by granular landslides in complex geometries. Thus, it aims at maximizing near-field accuracy while minimizing computational costs, thereby enabling efficient far-field wave propagation. This strategy involves using the 3D model (OpenFOAM®) where nonlinear and confinement effects are dominant and feeding the 2D model (Mild Slope Equation) where the waves can efficiently be handled by such simplified tool. This model chain has been applied to the 2015 Taan Fiord, Alaska (USA), landslide-tsunami event, a complex and well-documented case, with extensive field data available. Beyond evaluating its performance for this specific event, the broader aim is to provide some general insights and practical guidance for the application of this modeling chain to landslide-tsunami events. To this end, a sensitivity analysis, by varying the position of the coupling boundary between the two models, is also presented and discussed.

Plain Language Summary In this paper, a coupling strategy between 3D and 2D models for simulating tsunamis induced by granular landslides in complex geometries is proposed. The aim of this strategy consists in maximizing near-field accuracy while minimizing computational costs, thereby enabling efficient far-field wave propagation. The proposed approach involves using the 3D model (OpenFOAM®) where nonlinear and confinement effects are dominant and feeding the 2D model (Mild Slope Equation) where the waves can efficiently be handled by such simplified tool. To demonstrate the capabilities of the proposed model chain, it is applied to the 2015 Taan Fiord, Alaska (USA), landslide-tsunami event. It features both near-field challenges, due to the confined fjord geometry, and far-field propagation affecting nearby coastlines. This case is complex and well-documented, with extensive field data available to support the modeling and enable validation. Based on the results, the accuracy of the proposed coupling methodology is assessed. Although the results and the related discussions presented in this work are strictly related to the Taan Fiord case, the methodology presented could offer some general insights and practical guidance for the application of this modeling chain to landslide-tsunami events in complex geometries.

1. Introduction

Tsunamis generated by landslides represent a significant hazard, specifically in coastal, fjord, and lake environments, where submarine and subaerial mass movements can trigger destructive waves. Unlike tsunamis caused by seismic activity, landslide tsunamis often exhibit localized yet extremely high runups, representing very serious threats to nearby populations and infrastructures. Historical events, such as the 1958 Lituya Bay megatsunami (Alaska, Fritz et al., 2009) and the 2018 Anak Krakatau tsunami (Indonesia, Grilli et al., 2019), highlight how devastating can be the impact of such phenomena, highlighting the need for a thorough understanding of their dynamics.

Writing – original draft: A. Romano, C. Cecioni, G. Bellotti, G. Barajas, J. L. Lara
Writing – review & editing: A. Romano, C. Cecioni, G. Bellotti, G. Barajas, J. L. Lara

The accurate modeling of tsunamis generated by landslides is crucial for activities such as risk assessment and the preparation of mitigation strategies, including the development of hazard maps and tsunami early warning systems (Cecioni et al., 2011; Grilli et al., 2009, 2017; Løvholt et al., 2020). The nature of these hydromorphodynamic processes is complicated, as it involves a violent interaction between a slide mass and a water body. Fundamental insights into the physical processes have been obtained by several experimental campaigns (see e.g. Bullard et al., 2019; Di Risio, Bellotti, et al., 2009; Di Risio, De Girolamo, et al., 2009; Enet & Grilli, 2007; Grilli et al., 2017; Heller & Spinneken, 2013, 2015; McFall & Fritz, 2016; Miller et al., 2017; Mohammed & Fritz, 2012; Mulligan & Take, 2017; Romano et al., 2013, 2016) and have guided the development of sophisticated numerical models, which are required to capture the various stages of wave generation, propagation, and runup.

Landslide-generated tsunamis can be numerically simulated using either three-dimensional (3D) computational fluid dynamics (CFD) or depth-integrated two-dimensional (2D) numerical models. Each approach has its strengths and weaknesses. 3D models are particularly valuable for capturing the complicated interactions between the landslide and the water, offering a detailed representation of tsunami generation processes. They are also capable of accurately simulating complicated highly nonlinear near-field wave phenomena, including wave breaking and runup along coastlines with complex geometries. However, the computational cost of 3D models is very high for simulating long-range wave propagation and therefore are suitable to model the very near-field, that is, small geographical areas. Example applications can be found in Abadie et al. (2010), Mulligan et al. (2020), Romano et al. (2020), Paris et al. (2021), Rauter et al. (2021, 2022), Romano et al. (2023).

Conversely, depth-integrated 2D models provide a more computationally efficient means of simulating tsunami propagation over large areas. These models may not capture the full complexity of the generation process with the same level of detail as 3D models, but are essential for far-field tsunami predictions. Although in some cases it is possible to directly account in these models for the wave generation phase (see e.g. Cecioni & Bellotti, 2010a, 2010b; Lynett & Liu, 2005), 2D models are not sufficiently accurate for simulating water entry problems and violent near-field interactions, especially in confined or complex geometries such as fjords.

In this paper, a coupling strategy between 3D and 2D models for simulating tsunamis induced by granular landslides in complex geometries is proposed. Thus, it aims at maximizing near-field accuracy while minimizing computational costs, thereby enabling efficient far-field wave propagation. This strategy involves using the 3D model where nonlinear and confinement effects are dominant and feeding the 2D model where the wave can efficiently be handled by such simplified tool. The selected models are the open-source OpenFOAM® (Romano et al., 2023) for near-field simulations and a full-frequency dispersive model based on the elliptic Mild Slope Equation (MSE), which is well-suited for reproducing at very low computation costs the propagation of small-amplitude waves in the far-field, including across oceanic scales (Bellotti et al., 2008; Cecioni & Bellotti, 2010b; Cecioni et al., 2011, 2023).

To demonstrate the capabilities of the proposed model chain, it is applied to the 2015 Taan Fiord, Alaska (USA), landslide-tsunami event. It features both near-field challenges, due to the confined fjord geometry, and far-field propagation affecting nearby coastlines. This case is complex and well-documented, with extensive field data available to support the modeling and enable validation (Haeussler et al., 2018; Higman et al., 2018; Lynett et al., 2025). The available data include post-event runup measurements, which are used to evaluate the model performances in the near-field. Additionally, tidal gauge data from a station approximately 160 km away offer insights into the far-field response. However, the recorded tsunami signal at this location is small (on the order of few centimeters) and mixed with other long-period waves of different origins. As the gauge is located within a small bay, a detailed analysis was performed to isolate the tsunami signal from other coexisting physical phenomena. Thus, this case can serve as a representative example of "complex" landslide-tsunami event.

On the basis of the results, the accuracy of the proposed coupling methodology is evaluated. Beyond assessing its performance for this specific event, the broader aim is to provide general insights and practical guidance for the application of this modeling chain to landslide-tsunami events. To this end, a sensitivity analysis, by varying the position of the coupling boundary between the two models, is performed.

The paper is structured as follows. After this introduction, the numerical models and the proposed coupling strategy are described. This is followed by an overview of the Taan Fiord case study, including a brief description of the event and of the available observational data. The coupling strategy used to reproduce the event is then

presented. A results and discussion section follows, assessing the effectiveness of the methodology. Conclusions close the paper.

2. Numerical Models

2.1. 3D Model: OpenFOAM®

In this section a brief description of the 3D numerical model is provided. As anticipated, this model is used to reproduce the landslide-tsunami generation, propagation and inundation in the near-field. Moreover, the 3D numerical results are used to feed the 2D model. To this end, the numerical modeling of tsunamis generated by deformable landslides is carried out with the OpenFOAM® platform (Jasak, 1996). IHFOAM (Higuera et al., 2013a, 2013b), based on *interFoam* of OpenFOAM®, can solve both 3D Reynolds-Averaged Navier-Stokes equations (RANS) and Volume-Averaged Reynolds-Averaged Navier-Stokes equations (VARANS) for two phase flows. RANS and VARANS equations are solved coupled to the Volume of Fluid (VOF) equation for accurately tracking the free surface elevation.

The RANS equations, used to model the flow at the clear fluid region, are based on the Reynolds decomposition, that identifies an average and a fluctuating component (i.e., velocity and pressure fields for incompressible models). These equations are represented by the mass and momentum conservation equations, coupled to the VOF equation as follows:

$$\frac{\partial u_i}{\partial x_i} = 0 \tag{1}$$

$$\frac{\partial \rho u_i}{\partial t} + u_j \frac{\partial \rho u_i}{\partial x_j} = -g_j x_j \frac{\partial \rho}{\partial x_i} - \frac{\partial p^*}{\partial x_i} - f_{\sigma i} - \frac{\partial}{\partial x_j} \mu_{\text{eff}} \left(\frac{\partial \rho u_i}{\partial x_j} + \frac{\partial \rho u_j}{\partial x_i} \right) \tag{2}$$

$$\frac{\partial \alpha}{\partial t} + \frac{\partial u_i \alpha}{\partial x_i} + \frac{\partial u_{ci} \alpha (1-\alpha)}{\partial x_i} = 0 \tag{3}$$

where u_i (m/s) are the ensemble averaged components of the velocity, x_i (m) the Cartesian coordinates, g_j (m/s^2) the components of the gravitational acceleration, ρ (kg/m^3) the density of the fluid, p^* the ensemble averaged pressure in excess of hydrostatic, defined as $p^* = p - \rho g_j x_j$ (Pa), being p the total pressure, α (−) the volume fraction (VOF indicator function) represents the proportion of each phase present in each cell. It varies from 0 to 1, and the sum of the contributions in a cell from the three phases is always 1, $f_{\sigma i}$ (N/m^3) the surface tension, defined as $f_{\sigma i} = \sigma \kappa \frac{\partial \alpha}{\partial x_i}$, where σ (N/m) is the surface tension constant and κ (1/m) the curvature (Brackbill et al., 1992). μ_{eff} (Pa · s) is the effective dynamic viscosity that is defined as $\mu_{\text{eff}} = \mu + \rho \nu_t$ and takes into account the dynamic molecular (μ) and the turbulent viscosity effects ($\rho \nu_t$); ν_t (m^2/s) is the eddy viscosity, which is provided by the turbulence closure model. Note that both that ρ and μ are functions of α. Finally, the compression velocity u_{ci} (m/s), a mathematical term used to ensure a sharp, well-defined interface between fluids, is calculated as $u_{ci} = \min[c_\alpha |u_i|, \max(|u_i|)] \frac{\frac{\partial \alpha}{\partial x_i}}{\left|\frac{\partial \alpha}{\partial x_i}\right|}$, where the compression coefficient c_α (–) is assumed to be 1 (Marschall et al., 2012; Weller, 2008). In the present 3D model, three phases (water, air and granular material) are considered. All the three phases are modeled as incompressible and immiscible fluids. Their behavior is modeled with the same mass and momentum equations (RANS) coupled with the Volume of Fluid (VOF) equation to model the interface among them. The standard OpenFOAM® solver named *multiPhaseInterFoam* is used as numerical solver, due to its ability to reproduce the behavior of three incompressible fluids, capturing the interfaces with the VoF method. For the three phases, the position of the interface is calculated by means of the MULES algorithm. As far as the turbulence is concerned, in this study the *k-ω-SST* turbulence model has been used, with the enhancement from Larsen and Fuhrman (2018) to deal with the overproduction of turbulence levels.

For the water and air phases, a Newtonian viscosity model is selected. The landslide is modeled as a granular material governed by a non-Newtonian Coulomb viscoplastic rheological model, which includes some basic features and observed phenomena in dense granular flows like the exhibition of a yield strength and a non-zero slip velocity (Domnik & Pudasaini, 2012). This rheological model, originally implemented and validated in OpenFOAM® by von Boetticher et al. (2016) in the solver *interMixingFoam*, has been implemented and validated

against three literature cases of landslide-tsunamis by Romano et al. (2023). So, the landslide is modeled as a fluid characterized by the corresponding dynamic viscosity μ_s defined as:

$$\mu_s = \mu_{\min} + \frac{p \sin(\delta)}{\|\mathbf{D}\|}\left(1 - \exp^{-m_y\|\mathbf{D}\|}\right). \tag{4}$$

where $\mu_{\min}$ is a minimal dynamic viscosity, p is the pressure, $\|\mathbf{D}\|$ is the norm of the strain-rate tensor, δ is the internal friction angle of the granular material, and m_y is a numerical parameter with units of seconds.

As stated, this non-Newtonian viscosity model (in which shear stress is not directly proportional to deformation rate) for sliding of dense granular flows has been added to the standard OpenFOAM viscosity library and linked to the standard OpenFOAM solver *multiPhaseInterFoam*, to simulate an immiscible sliding granular flow interaction with water, with an additional unmixed phase representing the air. This model, although simple, is characterized by a high flexibility and computational efficiency, depending only on few physics-based parameters. For further details, the reader is referred to Domnik and Pudasaini (2012), von Boetticher et al. (2016) and Romano et al. (2023).

This model has been recently used by Romano et al. (2025) and Abadie et al. (2025) to perform numerical analysis on energy mapping of tsunamis generated by subaerial granular landslides, investigating the energy transfer mechanisms between landslide and water waves.

2.2. 2D Model: MSE

This section describes the 2D numerical model, initially proposed by Bellotti et al. (2008), to reproduce the propagation of transient tsunami wave. The problem at hand is in general time-dependent; it is solved in the frequency domain and then transformed back in the time domain by means of the inverse Fourier transform.

Considering a Cartesian coordinate space (x, y, z) and assuming incompressible and inviscid fluid with an irrotational motion, the time dependent linearized three dimensional problem reads as:

$$\begin{cases} \nabla_h^2\phi + \phi_{zz} = 0 & \forall \quad (x,y,z) \\ \phi_{tt} + g\phi_z = 0 & \text{at} \quad z = 0 \\ \phi_z + \nabla_h h \cdot \nabla_h \phi & \text{at} \quad z = -h(x,y) \end{cases} \tag{5}$$

where ϕ is the fluid velocity potential, $\nabla_h = (\partial/\partial x, \partial/\partial y)$ is the horizontal gradient operator and the subscripts indicate the partial derivative. The problem defined by Equation 5 express the mass conservation, that is, Laplace equation, the linearized and combined dynamic and kinematic free-surface boundary condition at $z = 0$, and the bottom boundary condition, at $z = -h(x,y)$, being $h(x,y)$ the water depth.

This problem can be transformed in the frequency domain and then, for each frequency, can be solved analytically by separation of variable. Using the assumption of mildly sloping seafloor, and integrating over the depth the Laplace equation, the elliptic version of the MSE is obtained (see detailed derivation in Iorio et al., 2021). The MSE, expressed in terms of complex free-surface elevation $N(x,y;\omega_i)$ reads as:

$$\nabla_h[c_i c_{gi} \nabla_h N(x,y;\omega_i)] + k_i^2 c_i c_{gi} N(x,y;\omega_i) = 0 \tag{6}$$

with $\omega_i^2 = g k_i \tanh[k_i h(x,y)]$ the linear dispersion relationship. In Equation 6 $c_i = \omega_i/k_i$ and $c_{gi} = 0.5 c_i [1 + 2k_i h/\sinh(2k_i h)]$ denote respectively the phase and group velocity, with ω_i the ith angular frequency and k_i the relative wave number. The MSE (Equation 6) is solved using the finite element method, for all the frequencies resulting from the Fourier transformation of the time-dependent problem (Equation 5). The result in the time-domain can be recovered by taking the inverse Fourier transform of $N(x,y,\omega)$ to obtain $\eta(x,y,t)$.

Boundary conditions are detailed and discussed in Bellotti et al. (2008) and Cecioni et al. (2023). A general expression reads as

$$\frac{\partial N(x,y;\omega_i)}{\partial \vec{n}} + ik_i N(x,y;\omega_i)\,\frac{1-R}{1+R} = ik_i N^I(x,y;\omega_i), \tag{7}$$

where $\vec{n}$ is the direction normal to the boundary and R is the reflection coefficient of the boundary. Indeed, if $R = 1$ the condition induces a full wave reflection, while $R = 0$ is a fully absorbing boundary that can be used to approximate a radiating condition. It should be pointed out that Equation 7 assumes that there is no phase shifting between incident and reflected waves and that the incident waves have the same direction of $\vec{n}$. The right hand side term of the general boundary condition expressed in Equation 7 is non-zero only at the boundaries where a wavemaker condition is imposed. Indeed, $N^I(x,y;\omega_i)$ is the ith component of the Fourier transform of the incident free surface elevation $\eta^I(x,y,t)$ entering in the 2D domain. Further details on where these boundary conditions are applied are reported in Section 4.3.

The model was selected based on two specific characteristics that make it particularly well-suited for the intended purposes of the coupling strategy, namely: (a) it is very efficient from a computational point of view. Thus, it is a suitable numerical tool for propagating landslide-generated tsunami waveforms over very large distances from the source, including oceanic scales and megatsunami scenarios; (b) it is also highly effective for analyzing the natural modes response of geographical configurations that require a detailed assessment to interpret the complex physical phenomena that govern the tsunami characteristics. In fact, the MSE solved in the frequency domain (Equation 6) enables the investigation of resonance modes of bays, fjords, small volcanic islands, etc. Thus, the same model framework can be used both to simulate the propagation of the landslide-tsunami over large distances, and, by means of a frequency scanning procedure (see Section 3.3), to evaluate the tsunami amplification in complex geographical configurations.

2.3. 3D-2D Coupling

The coupling between the 3D and the 2D models is carried out at the interface boundary between the two numerical domains. Specifically, the two domains share at least one of the computational boundaries (i.e., the interface boundary) or, depending on the shape of the domain (as described later), are partially overlapped. Therefore, at the interface boundary, a radiation boundary condition is applied in the 3D domain, while a generation line (i.e., wavemaker boundary condition) is applied in the 2D domain and a free surface elevation time series (eventually variable in space), obtained from the 3D model, is used as input for the 2D model. It is important to highlight that the interface boundary should be ideally placed at the interface between the so-called near- and far-field. In fact, it is expected that nonlinear phenomena and site-specific effects, related to the confinement characteristics of particular topobathymetry configurations (e.g., a fjord), are dominant in the near-field. This aspect is particularly important, especially because in this work a linear model is applied for the far-field propagation. It is commonly recognized by the scientific literature that the definition of the so-called near-field can be quite ambiguous.

In fact, it is very difficult to define clearly the near-/far-field boundary based on the distance from the landslide impact point, and/or the characteristics of the impulsive wave signals, and/or the characteristics of topobathymetry and degree of confinement. This is a crucial aspect and must be carefully treated. In this work, in order to show the capability of the coupling strategy, the method is applied to simulate a case where the topobathymetry configuration is very complex, that is, the Taan Fiord, AK. Moreover, in order to cope with such uncertainty level, a sensitivity analysis on the distance of the interface boundary is carried out.

3. Description of the Taan Fiord (AK) Event and Field Data Used for Comparison With Model Results

3.1. The Taan Fiord (AK) Event

The October 2015 landslide-generated mega-tsunami in Taan Fiord, Alaska, is a well-documented event that provides valuable insight into the landslide properties and tsunami propagation across both near- and far-field regions (Haeussler et al., 2018; Higman et al., 2018; Lynett et al., 2025). Taan Fiord, a 17-km-long inlet off Icy Bay in southern Alaska, comprises two basins, northern (~100 m deep) and southwestern (~130 m), separated by a central ridge at ~50 m depth (Franco et al., 2021). The fjord's width varies from 1.0 to 1.5 km in the north to 2.0–4.5 km in the southwest, with a 2.7 km wide entrance. On 17 October 2015 at 9:18 p.m. local time (18 October

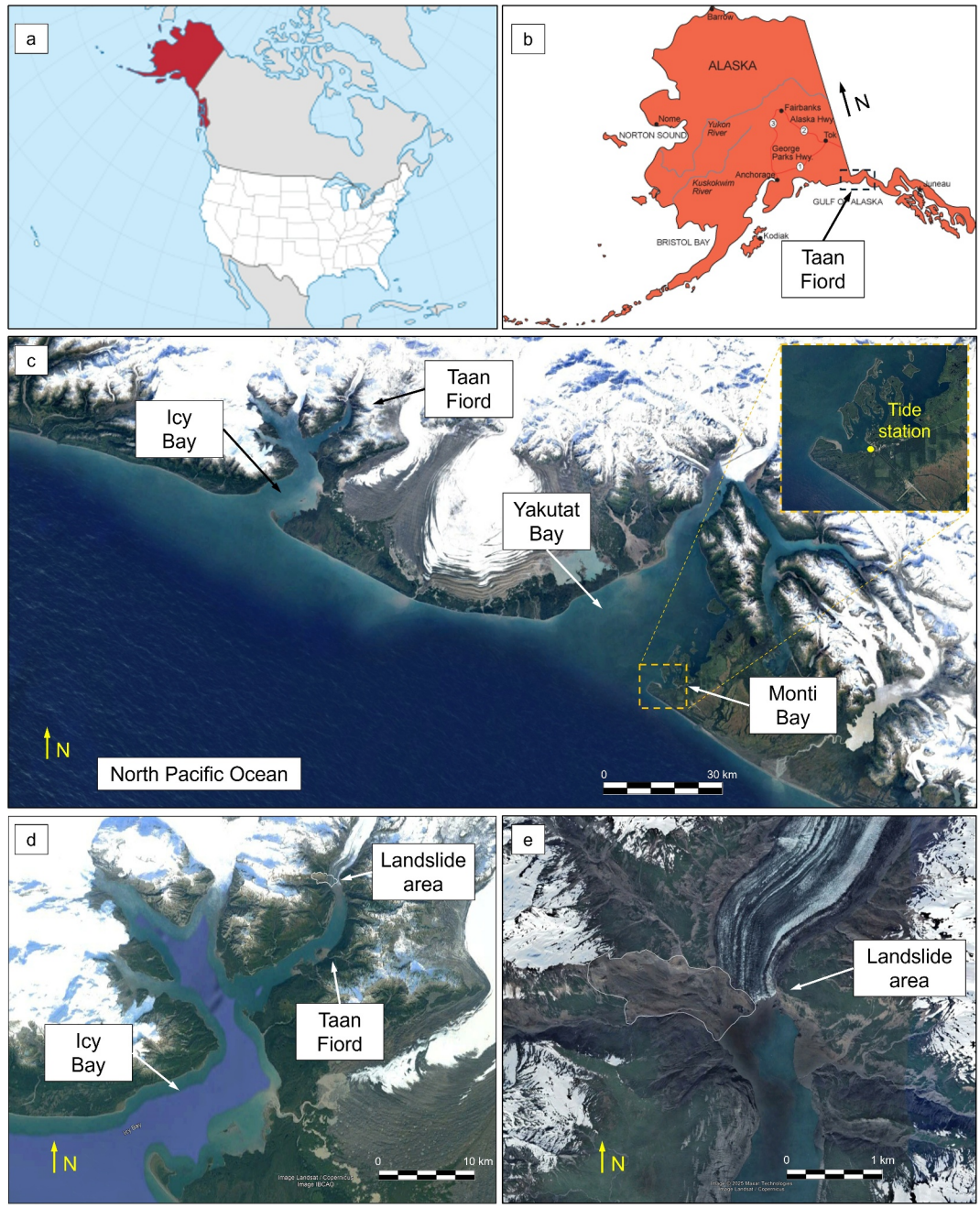

Figure 1. Location of Taan Fiord inside Icy Bay, Yakutat Bay, and Monti Bay (AK, USA; panels a–d), and area of interest in the 2015 Taan Fiord landslide event (panel e).

2015, 5:18 a.m. UTC) a subaerial landslide catastrophically failed at the northern tip of the Taan Fiord. Figure 1 reports the geographic location of the Taan Fiord (panels a–d) and the area of interest for the landslide event (panel e).

The landslide, with an estimated bulk density of 2,350 kg/m^3, mobilized 76 +3/−4 Mm^3 of material of which 51 Mm^3 deposited in the fjord, according to Higman et al. (2018) and Haeussler et al. (2018), who compared the pre-landslide topographic data set from a 2012 Digital Elevation Model (DEM) with the post-landslide comprehensive topographic and bathymetric data set from 2016. Some slide material did not enter the fjord but remained on the glacier and the bottom of the scar. Landslide and post-landslide deposits extended ~6 km down-fjord and

reached thicknesses of up to 70 ± 11 m, totaling ~147 Mm^3 (Haeussler et al., 2018), including fjord floor material mobilized and suspended as the slide entered and traveled down fjord. Later, Franco et al. (2021), who also modeled the landslide and the generated tsunamis using 3D CFD simulations (FLOW-3D) with granular flow models, calculated a landslide volume of 49.4 Mm^3, using the difference between the Arctic digital elevation model (DEM) from 2014 and the DEM data set 2016. Corsa et al. (2022) using DEMs from 2012 to 2019 calculated a landslide mobilized volume of 77. 0 ± 0.9 Mm^3, of which approximately 56.3 Mm^3 deposited in the fjord. Vegetation loss over 0.6 km^2, new return-flow channels, steep scarps (~10 m), and major delta reworking were documented (Bloom et al., 2020).

The impulsive waves generated by the landslide collapse propagated throughout Taan Fiord and Icy Bay, causing runup (Higman et al., 2018; Lynett et al., 2025), reaching a peak of ~193 m on a steep slope directly across from the landslide, ranking among the highest tsunami runups ever documented, and continued into the North Pacific Ocean, reaching, although significantly tamed in amplitude (i.e., few centimeters), the nearest tide gauge at Yakutat (AK), located in Yakutat Bay, 160 km to the southwest (see panel c of Figure 1).

3.2. Available Field Data

Following the 2015 event, Haeussler et al. (2018) conducted detailed post-event bathymetric surveys using multibeam sonar and high-resolution seismic data. These measurements allowed them to estimate the total volume of the landslide at 76 Mm^3, with an uncertainty of +3/−4 Mm^3. Of this, approximately 51 Mm^3 of material were deposited into Taan Fiord, reshaping the submarine morphology and contributing significantly to tsunami generation.

As for tsunami runup, in 2016 a multi-institutional team conducted three dedicated field surveys focused on identifying tsunami high-water marks and runup indicators. Runup measurements, presented by Higman et al. (2018) and later refined and integrated by Lynett et al. (2025) with survey data that have not been previously published, provide crucial insights into the spatial extent and energy of the tsunami triggered by the landslide. These field surveys documented maximum runup heights exceeding 190 m near the landslide source, making it one of the highest tsunami runups ever recorded. The high-resolution data also captured the variation in wave heights along the fjord and adjacent coastlines, offering essential validation for tsunami models and contributing to the broader understanding of landslide-generated wave behavior in glacial fjord settings. It should be noted that these data are currently one of the most complete and detailed benchmark data set of a mega-tsunami's onshore effects.

Additionally, tide gauge data from NOAA's Yakutat station (Yakutat, AK, NOAA Station ID 9453220), located in Yakutat Bay, Alaska (see panel c of Figure 1), recorded the far-field signal of the tsunami. Although the station is located approximately 160 km from the landslide site, the sea level data captured a subtle but discernible signal associated with the tsunami arrival. This instrumental record complements the field-based runup observations and provides temporal constraints on tsunami propagation, which are valuable for calibrating numerical models and assessing the broader regional impact of the event. Detailed analysis of the data is provided in the following Section 3.3.

3.3. Analysis of Tidal Gauge Data

As mentioned, NOAA's Yakutat station recorded the tsunami triggered by the 2015 Taan Fiord landslide event. The station is located within Monti Bay (59.55°N and 139.73°W), a small semi-enclosed area of approximately 15 km^2, located at the entrance of the larger Yakutat Bay (its position is shown in panel c of Figure 1 and later in Figures 3 and 8). The signal recorded by the station is reported in terms of water level (η_{wl}), in the upper panel of Figure 2 with a red line. The figure presents a 4-day record starting from 18 October 2015. Harmonic analysis of the observed water level was applied to identify the tidal component, η_a (blue line in the same panel). The residual component η_r (containing both storm surge and tsunamis signals; black line in the same panel) has been obtained, by removing η_a from η_{wl}.

The middle panel of Figure 2 reports the frequency spectrum of the η_r. It clearly shows that large amounts of energy are found in selected frequency bands. Notably, a very large peak exists for the lowest frequencies, that is, periods longer than 6 hr, which is assumed not related to the landslide-generated tsunamis that normally exist on

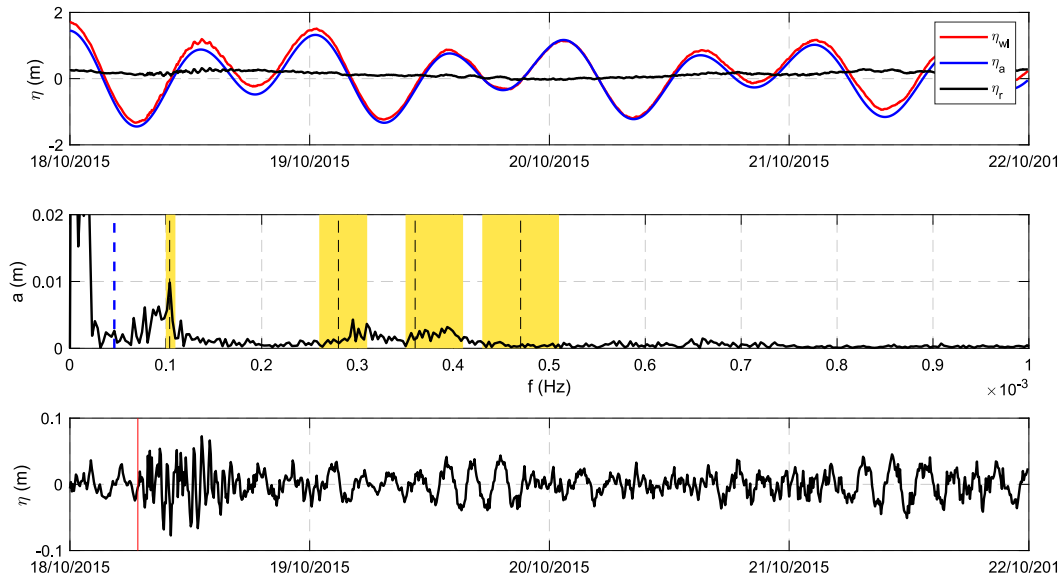

Figure 2. Upper panel: observed water level (red), astronomical tide (blue), and residual (black) time series at Yakutat tide station between 18 October 2015 and 22 October 2015. Middle panel: frequency spectrum of the residual time series. Note: vertical blue dashed line identifies the frequency used for the high-pass filter; vertical black dashed lines identify the $0.1{\cdot}10^{-3}$, $0.28{\cdot}10^{-3}$, $0.36{\cdot}10^{-3}$, and $0.47{\cdot}10^{-3}$ Hz modes of Yakutat Bay obtained by the modal analysis; yellow bands indicate the frequency limits of the bay's modes obtained performing the analysis considering the lowest and highest astromonical tide. Lower panel: high-pass filtered time series of the residual at Yakutat tide station between 18 October 2015 and 22 October 2015. The vertical red line denotes the tsunami arrival time.

higher frequencies. Therefore, a high-pass filter was applied to η_r, using a cut off frequency, $f_{cut} = 4.6{\cdot}10^{-5}$ Hz, corresponding to a 6 hr period and indicated by a vertical blue dashed line in the figure. In the following, it is assumed that these components cannot be related to the landslide-generated tsunamis, which normally exist on

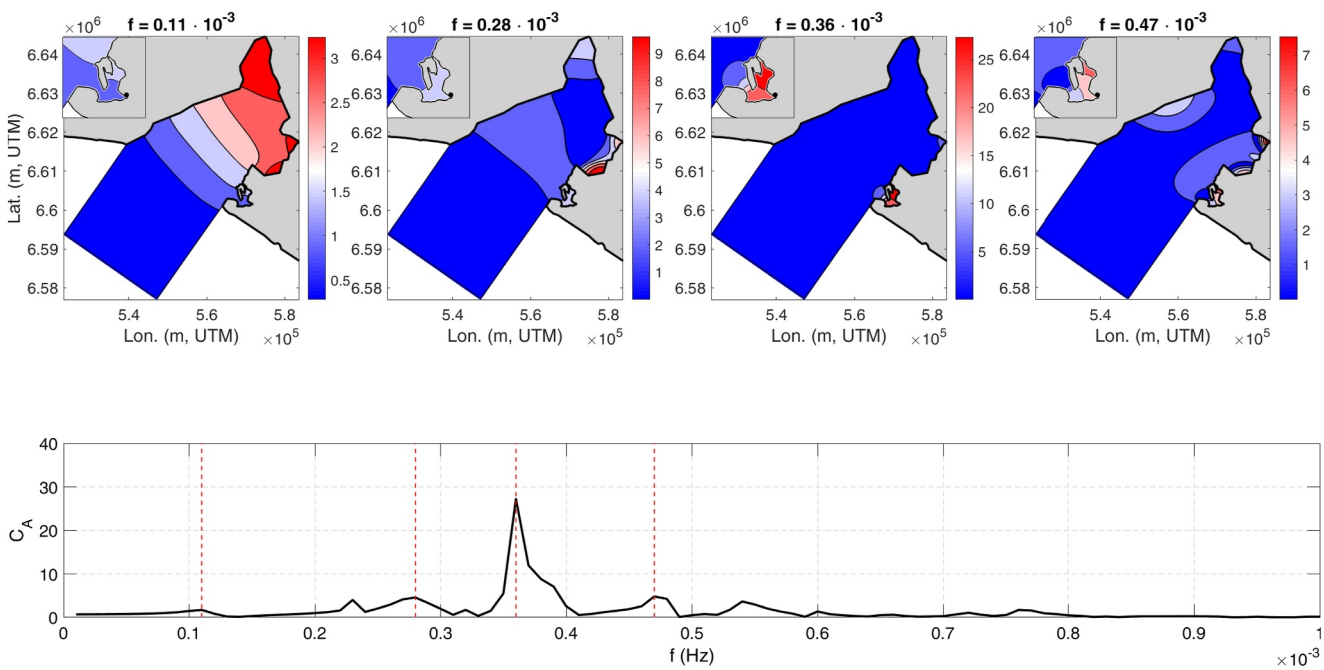

Figure 3. Amplification coefficient, C_A of the wave field. Upper panels: wave amplitude amplification C_A in Yakutat Bay (large images) and Monti Bay (insets) for the frequencies reported in the lower panel with vertical dashed lines. Lower panels: C_A for the lowest frequencies reproduced at the position where is located the Yakutat tide station.

higher frequencies. A high-pass filter was therefore applied to η_r using f_{cut} as cut-off frequency. The lower panel of Figure 2 shows the resulting filtered signal; the vertical red line indicates the tsunami arrival time, as determined by the 2D numerical simulation, presented in Section 5.2.

The spectrum of η_r shows at least three further peaks. It is now interesting to investigate if the corresponding peak frequencies are related to eigenmodes of the semi-enclosed sea areas in which the tidal gauge is located. This is important in order to understand if these dominating frequencies are directly related to the properties of the incoming landslide-generated tsunami waves, or if they are related to the resonating long waves in the bay.

To this end, two methods can be used. One is the modal analysis as proposed by Bellotti et al. (2012), already applied in similar geophysical applications (Aranguiz et al., 2019; Cortés et al., 2017; Sammarco et al., 2024). An alternative is to simulate the propagation of small amplitude waves, scanning the frequencies of expected interest, evaluating the response at the considered positions, looking for specific amplifications. The latter method has been selected, by applying the same MSE model described before and used also for the tsunami modeling in the far-field. The 2D numerical domain encompasses the Yakutat and Monti Bays. Note that these simulations are not intended to reproduce the tsunami itself, but rather to force the bays with unitary amplitude waves, imposed at the off-shore boundary. The aim is to identify amplifications due to resonance. Furthermore, given the complex/confined geometries of Monti Bay, wave trapping mechanisms could significantly influence tsunamis (Bellotti & Romano, 2017; Romano et al., 2013).

Figure 3 shows the result of this resonance analysis. The computational domain is illustrated in the upper panels of the figure, with a zoom-in on Monti Bay, shown in the up-left corner of each panel. The Yakutat tide station is marked with a black circle. The computation was carried out using a water level of 0.63 m below the mean sea level, corresponding to the sea level during the tsunami event. The lower panel of Figure 3 shows the amplitude coefficient C_A at Yakutat station as a function of the simulated frequency. Several amplification peaks are identified in the diagram. In particular, four frequencies, that is, $0.11{\cdot}10^{-3}$, $0.28{\cdot}10^{-3}$, $0.36{\cdot}10^{-3}$ and $0.47{\cdot}10^{-3}$ Hz, were identified as resonant modes and marked in the figure with vertical red dashed lines. The upper panels of the same figure illustrate the spatial patterns of C_A for these four frequencies using a color scale; note that the color scales differ between panels to enhance the visualization of the spatial shape of the modes.

The solution with $f = 0.11{\cdot}10^{-3}$ Hz is the first longitudinal mode of the Yakutat Bay. It shows a large crest at the northern edge, while a nodal line locates in correspondence of the separation with the open sea. The solution with $f = 0.28{\cdot}10^{-3}$ Hz is the second longitudinal mode of Yakutat Bay, with a crest in the northern edge and a trough at almost the entrance of the bay. The solution with $f = 0.36{\cdot}10^{-3}$ Hz is the Helmholtz mode of Monti Bay. A very large amplification of incoming waves can be expected in this case, as confirmed by the very large value obtained for C_A, in the order of 25. The solution with $f = 0.47{\cdot}10^{-3}$ Hz can be regarded as the sloshing mode of the small Monti Bay, with moderate amplification.

These four frequencies are then plotted in the middle panel of Figure 2, as black dashed vertical lines. Furthermore, yellow bands are included to represent the full frequency ranges where amplification occurs. The minimum and maximum frequency limits of these bands were determined by repeating the numerical simulation varying tide levels, specifically considering the lowest (−1.5 m) and highest (+1.5 m) astronomical tide respectively.

4. Models Coupling Application to Taan Fiord (AK) Event

4.1. Landslide Modeling

In this section a brief description of the procedure to estimate the initial landslide volume to be used for the following numerical simulations is provided. To this end, the pre- and post-event topobathymetric survey carried out by Haeussler et al. (2018) has been used. Panel a of Figure 4 shows the topobathymetry difference (Δz) before and after the 2015 Taan Fiord landslide event (Haeussler et al., 2018; Higman et al., 2018). In the same panel the landslide boundary polygon and the pre-event shoreline of the fjord are represented with dashed and continuous lines, respectively. The landslide boundary polygon is an irregular boundary derived from visual interpretation of satellite imagery captured after the landslide event. Its sole purpose is to visually delineate the area of interest for the subsequent reconstruction of the landslide volume and sliding surface. The other panels of the same figure (panels b–e) present an example of the procedure adopted to reconstruct the landslide volume and the pre-event

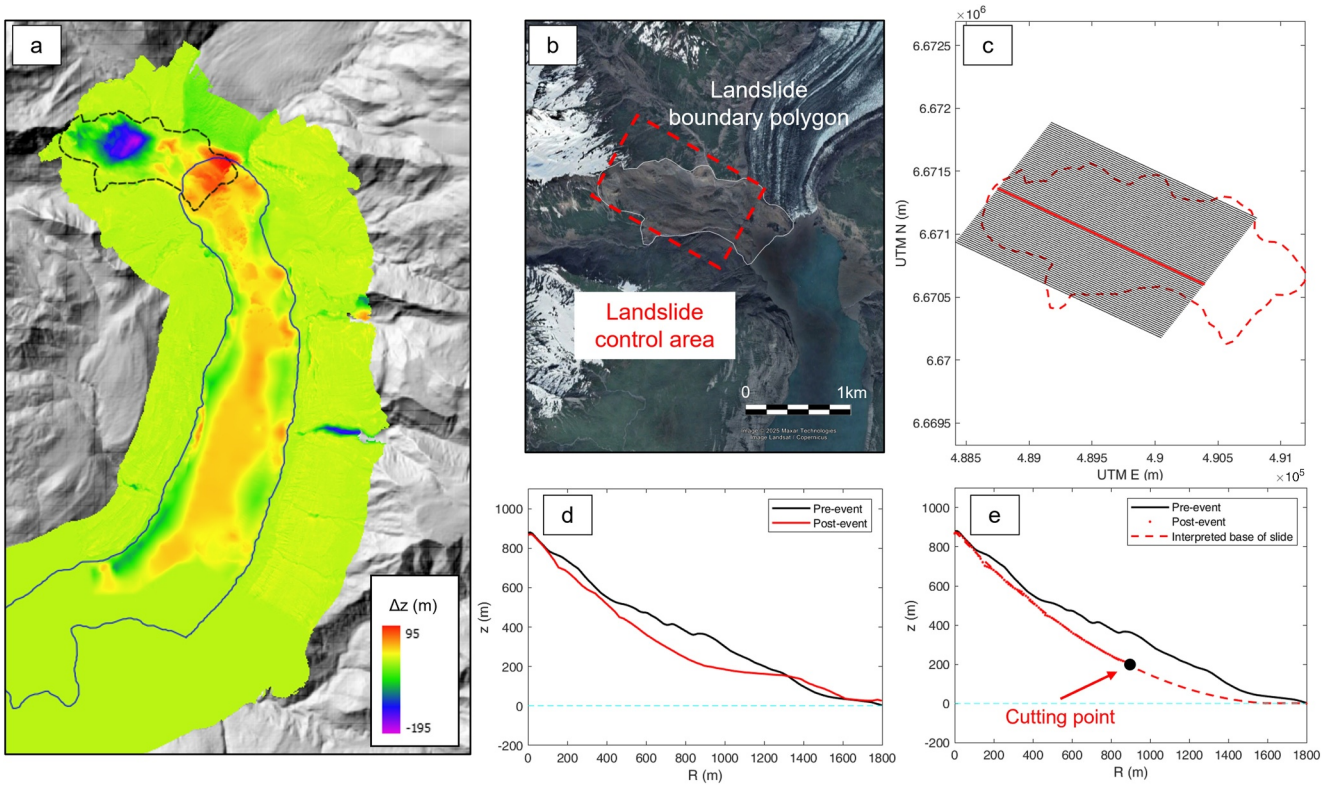

Figure 4. Panel (a): Topobathymetry difference (Δz) before and after the 2015 Taan Fiord landslide event (Haeussler et al., 2018). In the same panel the landslide boundary polygon and the pre-event shoreline of the fjord are represented with dashed and continuous lines, respectively. Panels (b–e): example of procedure to reconstruct the sliding surface (red dashed line in panel e) based on the analysis of pre- and post-event (black and red lines in panel d, respectively) topobathymetry survey within the landslide control area (panels b and c).

topobathymetry with sliding surface. Specifically, within the landslide control area, which consists of a regular grid (red dashed line in panel b), a series of cross sections, parallel to the main axis of the landslide and spanning 10 m apart, have been defined (panel c) and the pre- and post-event topobathymetry survey have been analyzed. Each cross section has been visually analyzed aiming at identifying a cutting point (panel e). Downstream of the cutting point, the post-event survey has been discarded. Upstream of the cutting point, the post-event survey has been used for interpolation with a polynomial curve, providing an "interpreted" base of the landslide (red dashed line in panel e): that is, sliding surface. Obviously, on the lateral edges of the control area often the interpolation is not necessary, as it is enough to merge the pre- and post-event topobathymetry.

This procedure, repeated for each cross section in the landslide control area and shown from different angles in panel a of Figure 5, allowed to obtain through interpolation: (a) landslide initial volume and (b) pre-event topobathymetry with sliding surface (see Figure 5). The initial landslide volume obtained in the present work (see panel b, c and d of Figure 5) is in the order of 81 Mm^3, which is comparable to that estimated by Haeussler et al. (2018) (76 +3/−4 Mm^3). These data represent the input for the 3D simulations.

In the next sections, the 3D-2D coupling strategy and the numerical setups for the considered case are described in detail both separately and from a coupling perspective. Nevertheless, it is useful at this stage of the manuscript to introduce the coupling approach for the Taan Fiord event. Figure 6 presents the sketch of the coupling between 3D and 2D domains (orange and blue dashed lines, respectively). In this case, due to the complex shape of the topobathymetry, the two domains are slightly overlapped. Moreover, the figure presents the location of the numerical wave gauges (yellow points) and the three zones (near, mid, and out; magenta squares) where numerical runup results are compared with runup surveys (Higman et al., 2018; Lynett et al., 2025). Note that the 2D domain is not fully represented in this figure, as it extends into Yakutat Bay, where the tidal station is located.

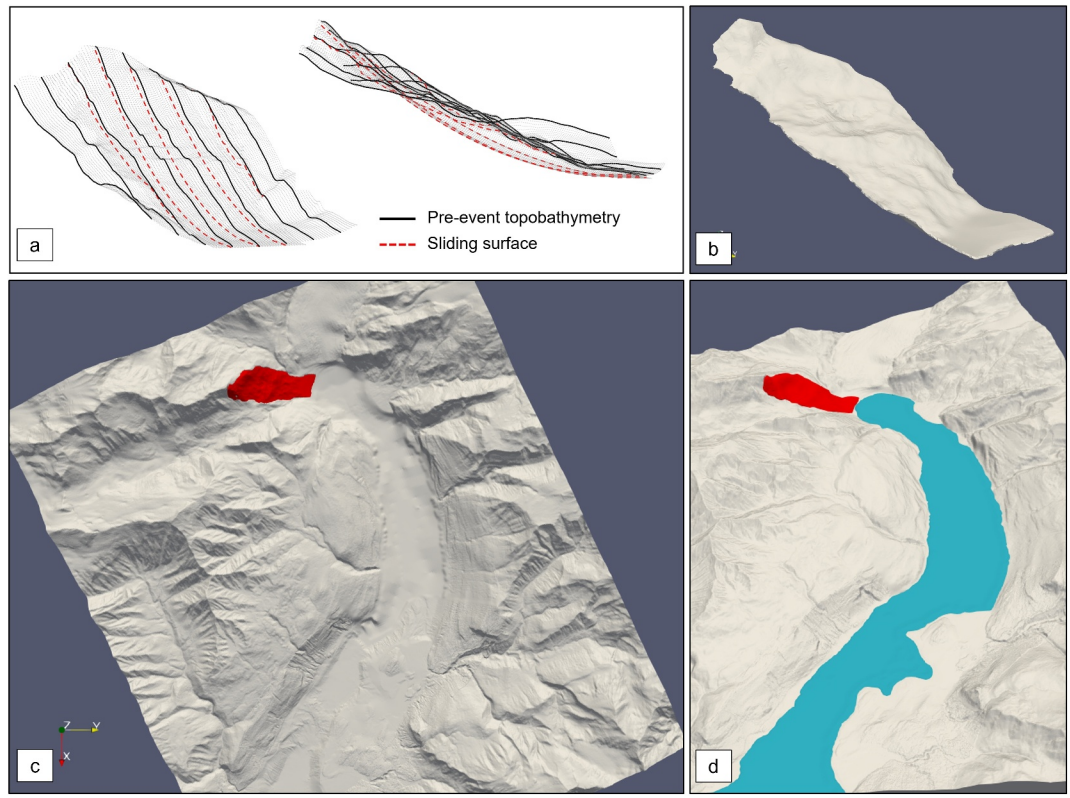

Figure 5. Reconstruction of landslide volume (panels a and b) and merging with pre-event topobathymetry with sliding surface (panels c and d).

4.2. 3D Model Setup

The 3D model domain, including the location where the free surface elevation time series and runup results are extracted, is shown in Figure 7. The domain has a length of 12,900 m, a width of 5,500 m and a height of 1,500 m. A body-fitted mesh has been used to improve the accuracy of the spatial discretization of the complex topobathymetry. Specifically, the STL file of the topobathymetry, combined with the *snappyHexMesh* library, is used to adapt the computational mesh to the shape of the fjord. The mesh resolution is not constant, as extra refinement zones, with $\Delta x = \Delta y \simeq 20$ m, $\Delta z \simeq 10$ m, are defined along the landslide path and around the undisturbed water free surface for a total number of ∼5M computation grid cells. These zones are identified by a change in the tone of the mesh color (see panel b of Figure 7). It is worth noticing that a previous convergence analysis of the computational mesh, not reported here, was carried out to tune the optimum value of the mesh size, trying to minimize the computational times, to be used for the simulations.

Impermeable frictional (*nutUWallFunction*) surface boundary conditions have been applied at the slope surface, at the bottom and at the walls of the computational domain. A radiating boundary condition has been applied at the southwest boundary to allow the exit of the waves from the computational domain. To improve the outward radiation of waves, the computational domain has been extended at a constant depth beyond the area of interest (see panels c and d of Figure 7) to minimize the numerical effects produced when the tsunami wave reaches the boundary. Clearly, the numerical results of this additional part of the domain are discarded. This is the reason why the two domains (3D-2D) are slightly overlapped (see Figure 6).

As for the rheological model of the granular material, the following parameters values have been used: slide density $\rho_s = 2{,}350$ kg/m^3, as estimated by Higman et al. (2018) and Haeussler et al. (2018), internal friction angle $\delta = 43.0°$, minimal dynamic viscosity $\mu_{\min} = 1e{-}6$ m^2/s. A previous sensitivity analysis of the internal friction angle, not shown here, was conducted to calibrate the optimal value of δ by constraining the numerical results using runup survey data at the "near" location. The simulations were performed using a desktop computer with the following characteristics: 13th generation Intel® Core™ i7-13700 CPU 2.10 GHz CPU unit, 64 GB RAM. The

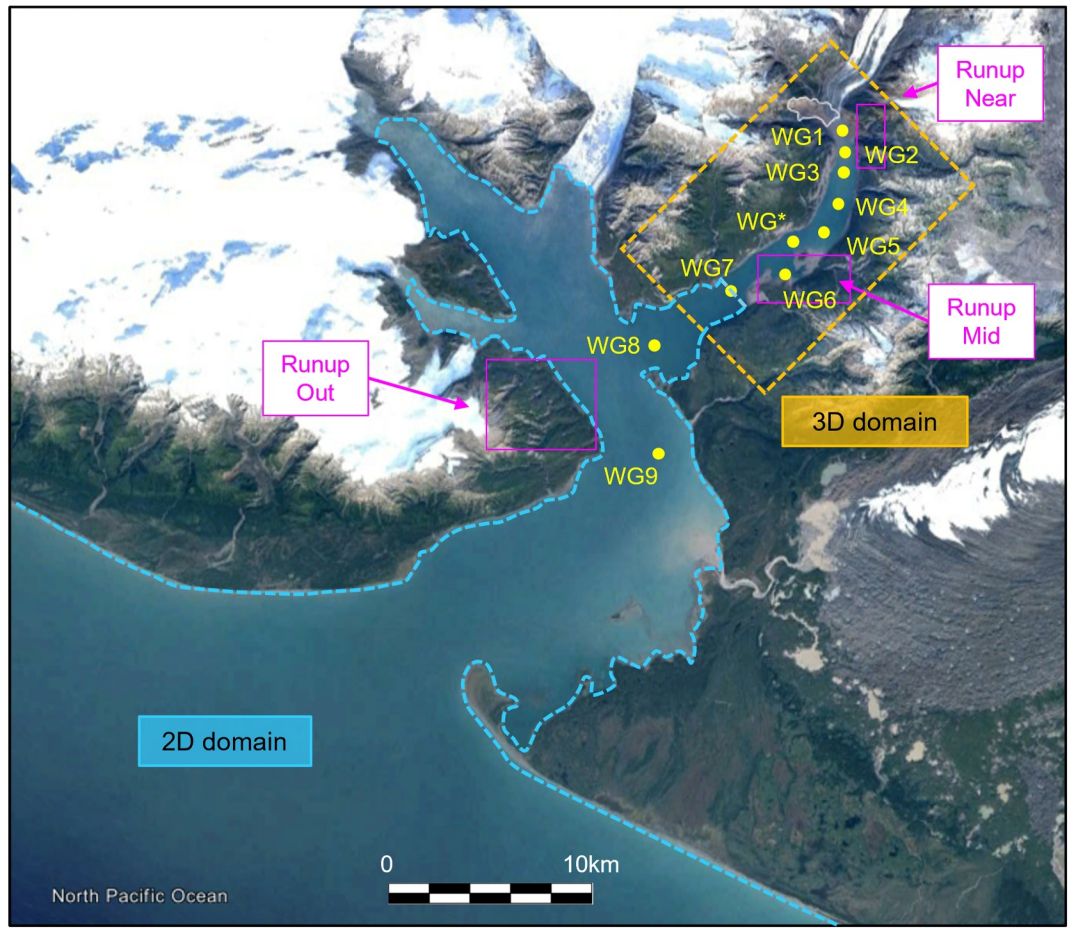

Figure 6. Sketch of the coupling between 3D and 2D domains (orange and blue dashed lines, respectively) for the Taan Fiord (AK), including the location of the numerical wave gauges (yellow points) and the three zones (near, mid, and out; magenta squares) where numerical runup results are compared with runup survey (Higman et al., 2018; Lynett et al., 2025).

numerical 3D mesh (~5M cells) was partitioned to be run in parallel in 16 processors, taking 15 days to numerically simulate 700 s.

3D model results have been saved in terms of free surface elevation time series at the locations indicated in Figure 6 as WG1, WG2, WG3, WG4, WG5, WG*, WG6, and WG7. Moreover, numerical free surface elevation is extracted via interpolation, for each time step, at the same coordinates of the survey runup data (Higman et al., 2018; Lynett et al., 2025). Then, for each considered point the maximum runup is identified at the locations "near" and "mid" (see Figure 6) for the subsequent comparison with the related survey point.

4.3. 2D Model Setup

The 2D model domain is shown in panel a of Figure 8. The domain includes the Icy Bay, where Taan Fjord is located, and the southern Yakutat Bay, where the NOAA's tidal station is located. The domain covers 8,840 km^2. Panel (a) of Figure 8 reports also the bathymetry of the area, referenced to the sea level during the tsunami propagation event, that is, 0.63 m below the mean sea level. The tsunami propagation has been reproduced for a simulation time of 100,000 s, that is, about 28 hr, which is long enough to allow waves to reach Yakutat Bay and to completely exit from the domain. A time step of $\Delta t = 1$ s is used, resulting in a total of $M_t = 100{,}001$ time steps. Applying the Fourier transform to the numerical problem with the above length in time and Δt, it results that in the frequency domain the resolution is $\Delta\omega = 2\pi/\Delta t/M_t = 2\pi 10^{-5}$, and the frequency range $\omega_i \in [0, (M_t - 1)\ \Delta\omega] = [0, 2\pi]$. However, as explained in Cecioni et al. (2023), the tsunami energy exists only on a specific band of the overall spectrum. After careful inspection of the spectrum of N^I, it has been concluded that the range of angular

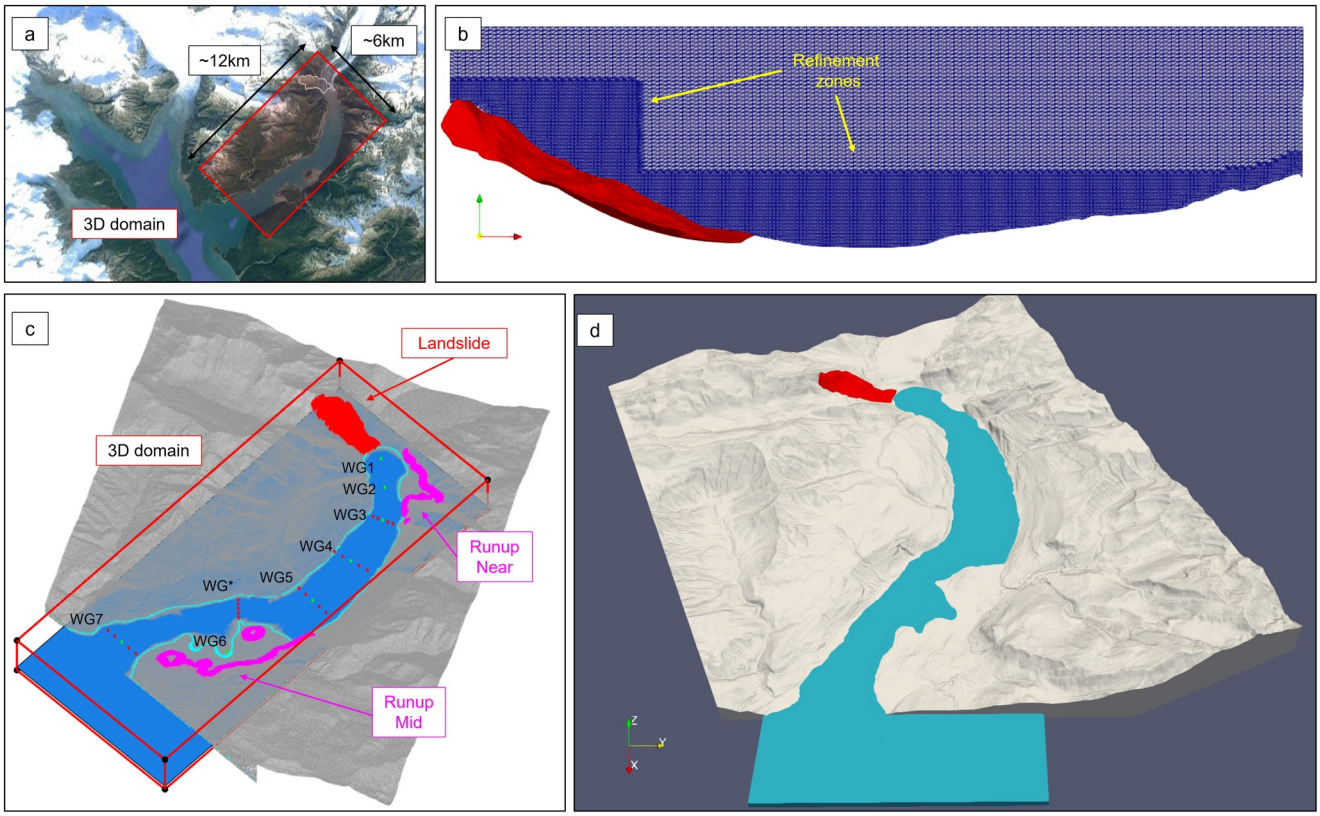

Figure 7. Panels (a) and (c): sketch of the 3D domain including the location where the free surface elevation time series and runup results are extracted. Panel (b): cross section, parallel to the landslide path, of the computational mesh used for the 3D simulations. Note that extra refinement zones are used along the landslide path and around the undisturbed water free surface. Panel (d): aerial view of the 3D domain used to model the landslide-tsunami propagation and inundation along the fiord. The initial position of the landslide volume is reported in red in panels (c) and (d).

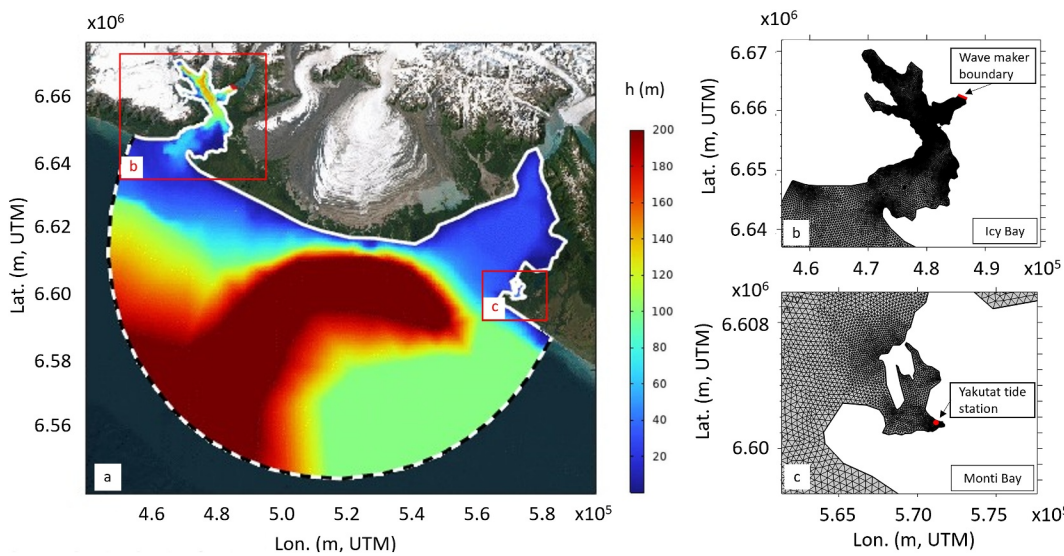

Figure 8. Panel (a): sketch of the whole 2D domain spanning from Taan Fiord and Icy Bay up to Yakutat Bay and contour of the related bathymetry. Examples of the FEM computational mesh used for the 2D simulations are reported in panels (b) and (c) for the areas of Icy Bay and Monti Bay, respectively. Panel (b) includes the position of the wave maker boundary (i.e., 3D-2D boundary interface), while panel (c) includes the position of Yakutat tide station in Monti Bay.

frequencies to be solved is between 0 and 0.02π. The computational mesh has been generated ensuring that the shortest waves, that is, those with the angular frequency of 0.02π, are solved with at least 10 nodes for wavelength. The simulations were performed using a desktop computer with the following characteristics: 13th generation Intel® Core™ i7-13700 CPU 2.10 GHz CPU unit, 32 GB RAM. The numerical 2D mesh results in ∼113k of Degrees of Freedom (DOF), taking for the solution of the 1,001 elliptic equations (one for each frequency) a total computational time of ∼30 min to numerically simulate about 28 hr.

In panel (a) of Figure 8, the continuous white line denotes the coastline boundary, where a partial reflection condition is imposed, using Equation 7 with $R = 0.9$ and $N^I = 0$. The dashed white line denotes the open sea boundary, where a radiation condition is applied ($R = 0$ and $N^I = 0$). Panels (b) and (c) provide a closer view of the Icy and Monti bays respectively. In panel b, the boundary where the radiation-wavemaker condition ($R = 0$ and $N^I(x, y; \omega_i) = 2N^{3D}(x, y; \omega_i)$) is applied is indicated with a red line: it represents the interface between the 3D and 2D models and it is located at the position of the wave gauge WG7, see Figure 6. The reason why a radiating condition is used, is to let the waves eventually reflected at the fjord coastline, to exit the domain and simulate the backpropagation toward the generation area. Note that in Section 5.3, a sensitivity analysis on the position of the coupling interface is carried out.

Panels (b) and (c) of Figure 8 provide an example of the finite element mesh resolution. It is coarser at large water depths and finer at coastal areas. In order to satisfy the minimum size requirements, the mesh elements size ranges between 1,000 and 70 m.

2D model computes the free surface elevation time series in all the nodes of the computational domain; however, for the present application, results are only extracted at the locations indicated in Figure 6 as WG7, WG8, and WG9 and at the location of the Yakutat tide station.

The 2D model cannot properly reproduce the coastal runup, since it is based on a linearized equation and the computational domain has fixed boundaries. Therefore, the semi-empirical formula of Madsen and Fuhrman (2008), based on Green's law and the surf similarity parameter ξ, is used to estimate the maximum runup values R_u. Its application is based on the wave properties evaluated at some extraction points (see Cecioni et al., 2023) in front of the coast. This formula reads as follows:

$$\frac{R_u}{A_p} = 2\pi^{3/4}\left(\frac{A_p}{h_p}\right)^{-1/4}\xi^{-1/2}, \tag{8}$$

where $A_p = H_p/2$ and h_p are the maximum incident tsunami wave amplitude and water depth, respectively, at the extraction locations, $\xi = \overline{\alpha}/\sqrt{H_p/L_0}$, with $\overline{\alpha}$ denoting the average bottom slope between h_p and the coast and L_0 the deep water wavelength. For the present application, considering the rather steep and shore-parallel bathymetry of the fjord around the "out" location of runup data, 41 extraction points were selected along the 50 m isodepth line, spaced at equal intervals of 100 m. Therefore, the free surface elevation time series solved by 2D model at these points, have been analyzed by a zero-crossing water surface analysis to evaluate the maximum apparent incident wave height (H_p), to be used in Equation 8.

5. Results and Discussion

5.1. 3D Results (Near-Field)

In this section the description of the 3D model results of the Taan Fiord landslide-tsunamis is provided. These results are presented to describe both the characteristics of the tsunamis in the near-field, comparing also the numerical results with survey data, and aiming at providing the input for the 2D model, used to reproduce the tsunamis in the far-field.

First the, landslide evolution is presented and discussed in Figure 9. The figure reports six selected time stacks ($t = 0$, 100, 200, 300, 500, 700 s) of the contour map of the landslide evolution. Note that in this figure, as well as in all the analysis presented throughout the article, the time is measured from the time at which the landslide is triggered ($t = 0.0$ s). Moreover, the color map refers to the elevation z (in m) measured from the undisturbed water level ($z = 0.0$ m). After the landslide triggering, the landslide volume enters quickly the fiord, interacting with the water body and generating the impulsive waves (described later). Most of the landslide displacement takes place

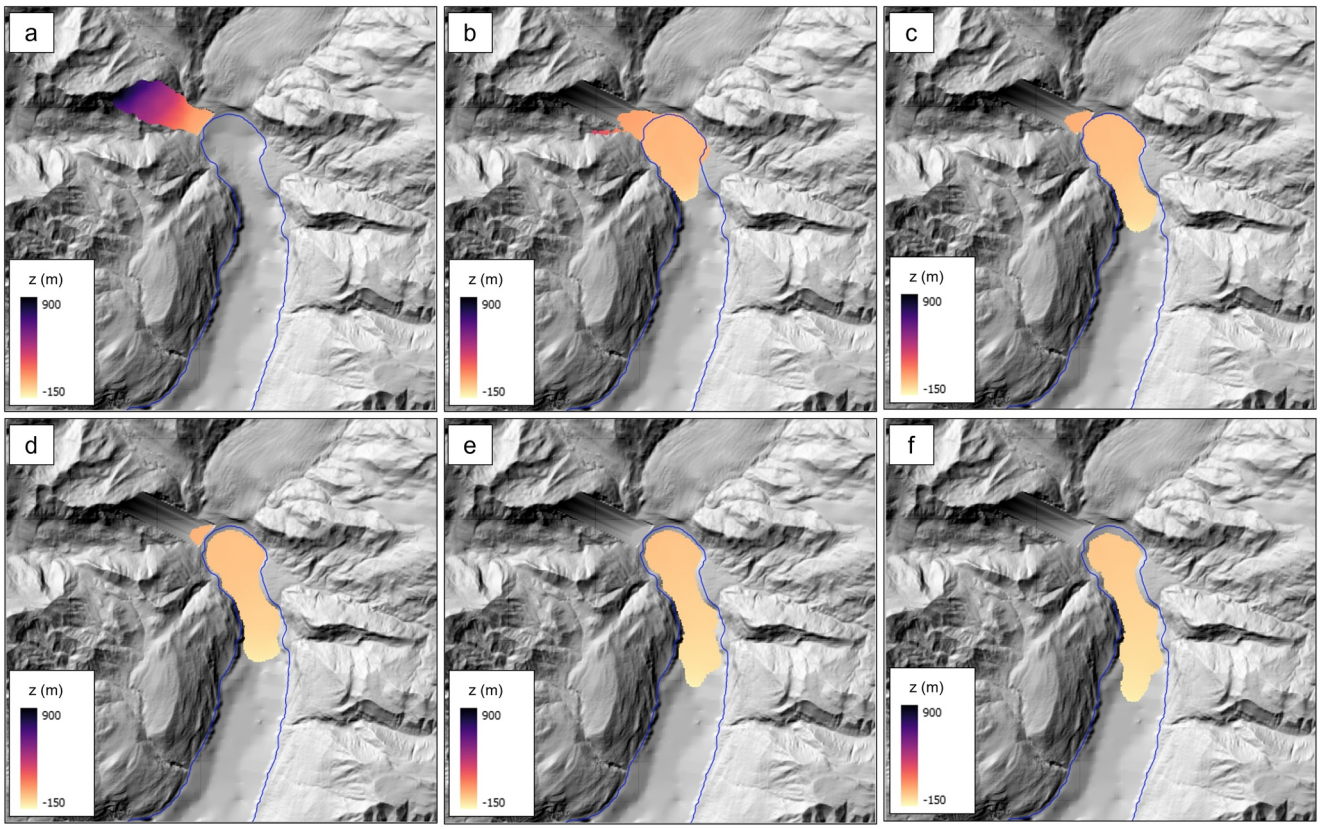

Figure 9. Selected time stacks (t = 0, 100, 200, 300, 500, 700 s; panels a–f) of the landslide evolution. Note: time instants are measured from the time at which the landslide is triggered (t = 0.0 s). Color map refers to the height z (in m) above/below undisturbed water level (z = 0.0 m) of the landslide.

during the first 150–200 s (panel c). Then, the landslide evolution slows down and viscous/creep movements continue throughout the simulation time until a steady state is reached (panel f).

As stated, when the subaerial landslide volume enters the water body, impulsive waves are generated. This process is shown in Figure 10, where selected time stacks of both landslide (in red) and the water (color maps refer to the water velocity magnitude) evolution are represented. The complexity of this well-known physical process, together with the following propagation and inundation phenomena, is magnified by the shape of the fjord's topobathymetry. The landslide enters the water and the first wave crest is generated by the typical piston-like mechanism (panel a). Immediately, the wave crest starts to propagate, interacting with the lateral banks (panel b) and the V-shaped valley placed in front of the landslide impact point (panel c), causing extreme runup. Then, the tsunami starts to propagate in the first part of the fiord's branch, characterized by steep lateral banks (panels d and e), that favor the inundation taming. After approximately 200 s from the landslide triggering, the first wave crest reaches a shallow area (panel f), where the width and the water depth of the fjord decreases abruptly (Franco et al., 2021), representing for the flow a "bottleneck." This is a tipping point for the characteristics of the tsunami propagation in the fjord. The wave front splits into two components: one part bypassing, overtopping and inundating the shallow bank area, while the other part continuing its propagation in the fjord's main channel (panel g) and partially inundating the shallow waters area (panels h–j). Downstream of the bottleneck, the tsunamis bore, after inundating the shallow area, flows in toward the fjord's main channel, merging and interacting with the propagating waves (panels k and l). Thus, the wave packet propagates toward the fjord's entrance.

After the description of the tsunamis propagation in the fjord, the quantitative comparison between numerical and field data is presented and discussed. Numerical free surface elevation is extracted via interpolation, for each time step, at the same coordinates of the survey runup data (Higman et al., 2018; Lynett et al., 2025). Then, for each considered point the maximum runup is identified and compared with the related survey point. Figure 11 presents a global comparison between survey and numerical runup, specifically at the locations "near" and "mid"

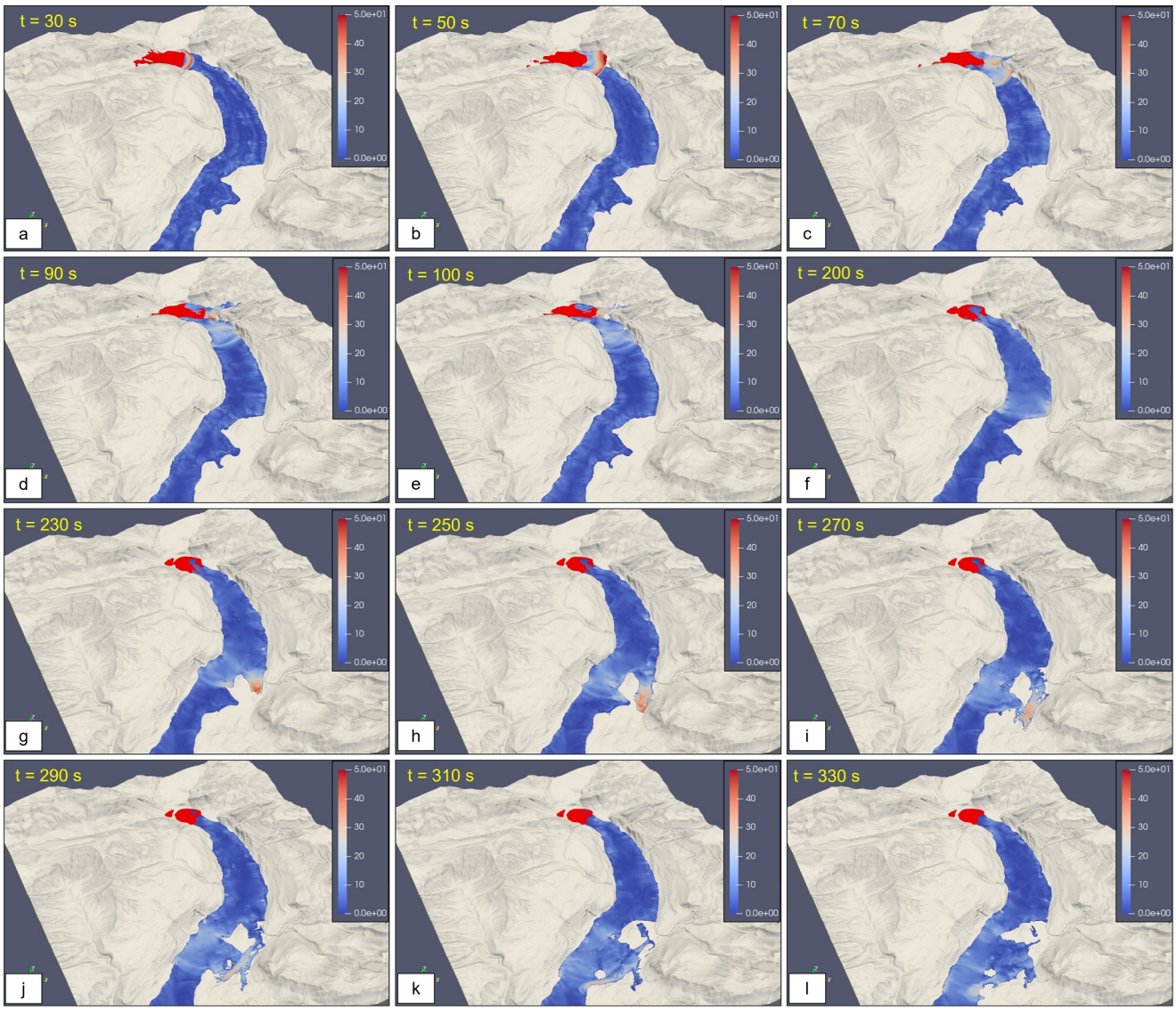

Figure 10. Selected time stacks (panels a–l) depicting the landslide-tsunamis generation, propagation and inundation along the fiord branch. Note: time instants are measured from the time at which the landslide is triggered ($t = 0.0$ s). Color maps refer to the water velocity magnitude (m/s). The bright red shape represents the landslide.

(see Figure 6). In the figure, for each runup survey point, the numerical flow elevation is represented with different colors, that describe the agreement between numerical and survey runup value at the considered point, namely: numerical overestimate and underestimate, are depicted with red and blue lines and markers, respectively, while gray lines and markers indicate survey points for which interpolation of numerical data did not yield results. Moreover, in the figure the initial positions of the shoreline and the landslide are represented with continuous black lines and shape, respectively.

Figure 11 is useful to provide a general comparison between the two sets of data. Nevertheless, to favor a more accurate comparison between survey and numerical runup data, considering also the different locations, Figure 12 is used. This figure presents a detailed comparison between numerical and survey runup at the location "near" (panels a and b) and "mid" (panels c and d) as a function of the distance D (measured from the slide back edge). Moreover, the comparison is presented in terms of both runup absolute values (η_R; panels a and c) and absolute differences ($\Delta\eta_R$; panels b and d). The color code is identical to that used in Figure 11, with two additional quantities, namely: (a) in panels a and c the absolute values of runup survey are represented with black lines and

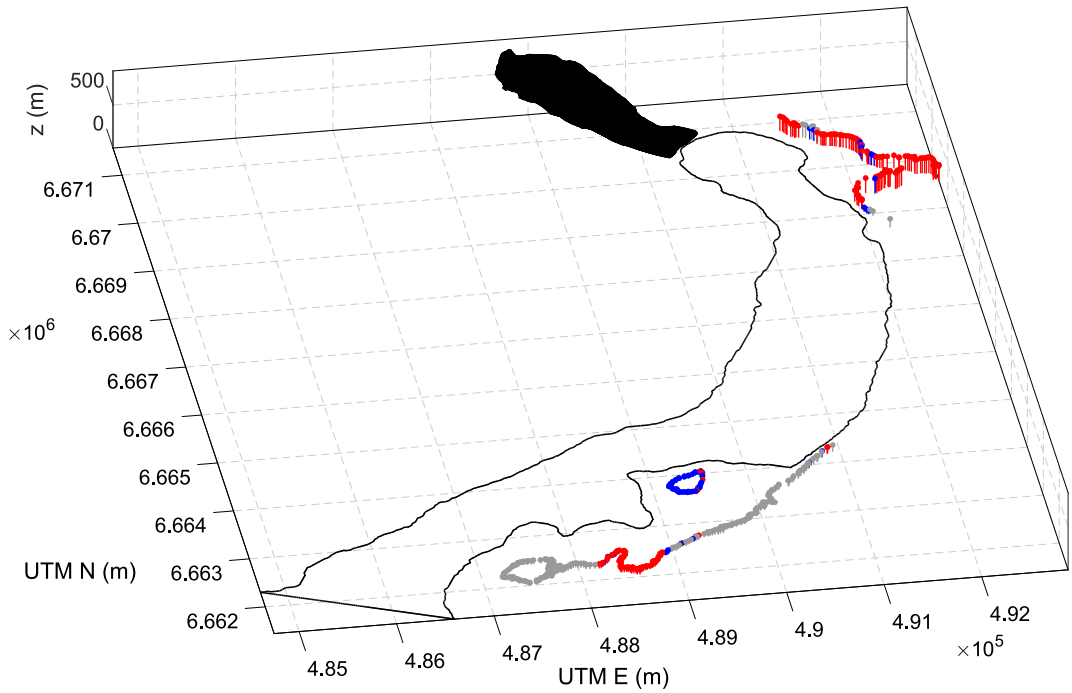

Figure 11. Comparison between numerical and survey runup ("near" and "mid" locations) in the 3D domain. Color code: numerical overestimate and underestimate are depicted with red and blue lines and markers, respectively, while gray lines and markers indicate survey points for which interpolation of numerical data did not yield results. Undisturbed shoreline and landslide initial positions are represented with continuous black lines and shape, respectively.

full circles; (b) in panels b and d gray dashes provide an estimate of the mesh vertical resolution: lower/upper hypens refer to $\Delta\eta_R \mp \Delta z$. Note that the mesh resolution is not uniform, as additional refinement zones are defined. Thus, although Δz is not constant throughout the domain, the dashes provide, on average, a representative visualization of the vertical mesh resolution. Moreover, the numerical results have been processed to extract in each computational point, for each time step, the flow extent/distance and elevation. Thus, the asynchronous inundation map has been obtained and represented in Figure 13, where the color map refers to flow elevation, that is, the height reached onland by the free surface elevation measured from undisturbed water level $z = 0.0$ m (η_R). Undisturbed shoreline and maximum inundation distance are represented with blue and red lines, respectively, while runup survey are plotted with magenta circles.

Figures 11–13 show a general good agreement between survey and numerical runup, as far as both runup extent and flow elevation are concerned. Specifically, in the "near" location, the numerical results well represent the whole runup survey pattern and the flow elevation, although exhibiting a general slight overestimate trend. This slight discrepancy might be due to the relevant sources of uncertainty that characterizes the process at hand. A significant source of uncertainty is related to the estimate of the volume and of the shape of the landslide. Another uncertainty factor is related to the modeling of the landslide. In fact, the landslide is reproduced as a homogeneous granular material governed by a simple rheological model, while in reality it is made of a heterogeneous medium, with mechanical characteristics that might vary both in space and time. This is clearly a simplification, as for the rheological model used the landslide material is globally described with few physical parameters. Therefore, it is possible that this global modeling could misinterpret the real slide dynamics over space and time, resulting, like probably in this case, in a slide which is less viscous than the real one, thus inducing larger waves and, accordingly, higher runup. Additionally, it is worth noting that all phases are modeled as immiscible fluids, which is another characteristic that could induce the generation of larger waves. Furthermore, these effects are magnified in the very near-field, where the interaction between landslide and water (i.e., wave-generation process) is characterized by a high variability in space and a quick evolution in time, especially in such a complex geometrical configuration. Apart from these discrepancies, the momentum exchange between landslide and water seems to be well reproduced. In fact, in terms of absolute difference (see panel b of Figure 12) and runup extent (see Figure 13) the discrepancies between survey and numerical data appear to be mild.

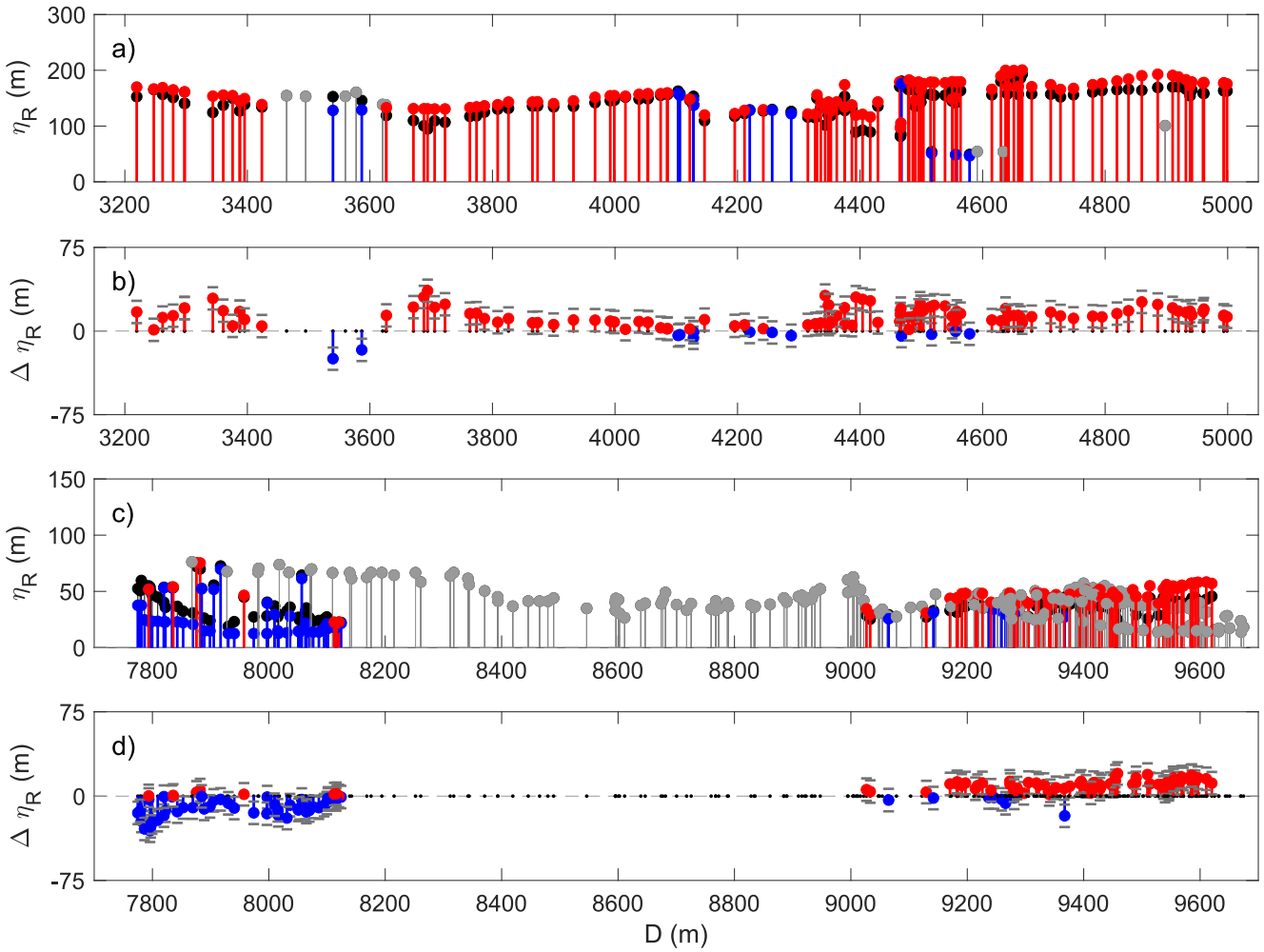

Figure 12. Comparison between numerical and survey runup at "near" (panels a and b) and "mid" (panels c and d) locations as a function of the distance D (measured from the slide back edge) in form of absolute values (η_R; panels a and c) and absolute differences ($\Delta\eta_R$; panels b and d). Color code: In the panels (a) and (c) runup survey are represented with black lines and full circles, numerical overestimate, and underestimate are depicted with red and blue lines and full circles, respectively, while gray lines and full circles indicate survey points for which interpolation of numerical data did not yield results. In the panels (b) and (d) gray dashes provide an estimate of the mesh vertical resolution: lower/upper hypens refer to $\Delta\eta_R \mp \Delta z$.

Similar considerations apply for the runup comparison in the "mid" location. Again a general good agreement between survey and numerical runup, in terms of both runup extent and flow elevation, is noticed. Nevertheless, comparing these results with that shown in the "near" location, a different behavior appears. In fact, the comparison between numerical and survey runup shows that in some areas the numerical data tend to overestimate the survey ones, while in others areas the trend is the opposite. Moreover, it should be mentioned that, contrarily to that observed in the "near" location, here the survey points for which interpolation of numerical data did not yield results appear to be more numerous (gray lines and markers in panel c of Figure 12). This aspect is likely related to further sources of uncertainty: (a) in this area, unlike the "near" location, the topobathymetry is characterized by very shallow and flat regions. Although the body-fitted approach aims to maintain and adapt the mesh resolution in both the horizontal and vertical directions, interpolation in these shallow/flat areas can be less accurate due to the coarser horizontal mesh resolution; (b) another source of uncertainty is related to the method used for obtaining the numerical data. This method is based on the extraction, for each time step, of the points cloud that represents the VOF water fraction equal to 0.5. This surface ideally represents the envelope, in the whole domain, of the water free surface elevation at the considered time step. This method has been selected, among others, due to its efficiency, accepting a margin of uncertainty and, to some extent, potentially reduced accuracy in certain regions. In fact, while this procedure provides a picture of the runup pattern in the whole domain, it can be less accurate when extracting the results at some specific points (i.e., survey points), especially in the "mid" location.

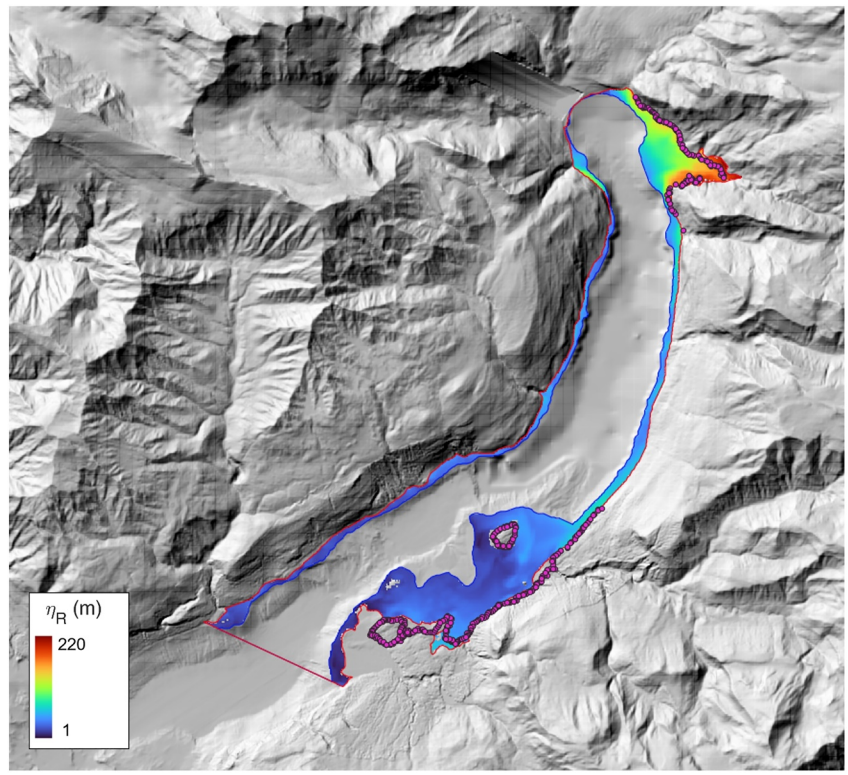

Figure 13. Numerical inundation map in the 3D domain. The color map refers to flow elevation, that is, the height reached onland by the free surface elevation measured from undisturbed water level $z = 0.0$ m (η_R). Undisturbed shoreline and maximum inundation distance are represented with blue and red lines, respectively, while runup survey are plotted with magenta circles.

Although this part of the domain is less sensitive to the initial conditions (i.e., effects of the landslide modeling for the tsunamis generation), it is characterized by a complex shape of the topobathymetry, in which both steep slopes and flat areas are present, and where the waves are smaller. Finally, it is worth noting that a qualitative comparison suggests that the inundated areas obtained in the present study (see Figure 13) are consistent with those reported in Figure 14 by Franco et al. (2021), especially in the "near" and "mid" locations.

To summarize, overall the tsunamis generation, propagation and runup phenomena are well caught by the 3D model, especially considering the factors that are expected to control this complex process. Despite the complex topobathymetry (see Figure 10), high degree of confinement, nonlinear effects, and the aforementioned sources of uncertainty, the numerical data well reproduce the survey runup pattern and flow elevations (see Figures 11–13).

Finally, the water free surface elevation and landslide thickness time series, measured at the eight gauges (WG1, WG2, WG3, WG4, WG5, WG*, WG6, and WG7) placed in the 3D domain as shown in Figure 7, are analyzed. These time series are represented in Figure 14. In the figure, the numerical time series of water free surface elevation and landslide thickness are plotted with red and gray lines, respectively. As far as the water free surface elevation time series are concerned, in the very near-field close to the landslide impact point (WG1), the wave signal is very sharp, closely resembling a solitary wave. The maximum wave crest, occurring after 25 s from the landslide triggering, is in the order of 80 m. A similar behavior can be noticed for the wave signal measured at WG2, which reaches a maximum value of 60 m. It should be mentioned that these values are very similar to those reported by Franco et al. (2021). In fact, they reported maximum wave crests in the order of 80–90 m at the wave probes P1b and P2 and of 60 m at P3. The positioning and numbering of these probes are reported in Figure 9, panels a, b, and d of Franco et al. (2021). Moving away from the generation area, the wave signal becomes less steep and the wave packet elongates. However, the complex interaction with the fjord's central ridge and the resulting inundation of the shallow area alter the nature of the signals, particularly downstream of the bottleneck (WG7). Thus, the free surface elevation time series measured at WG7 is used to feed the 2D model.

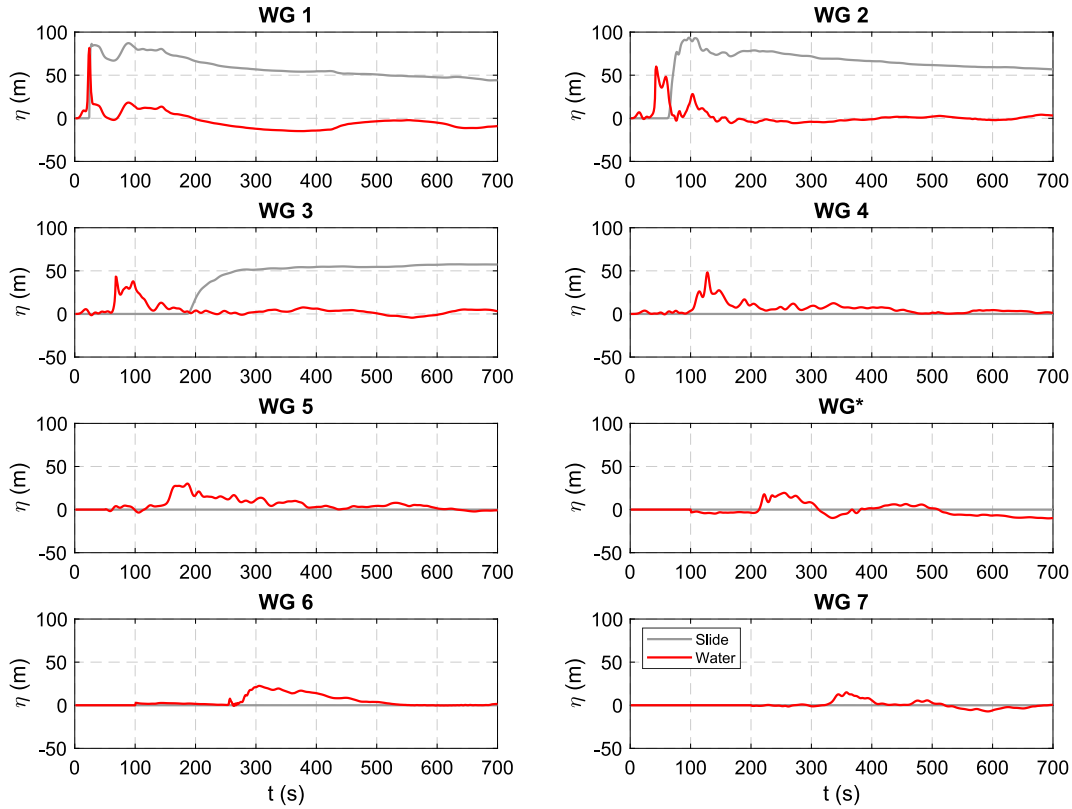

Figure 14. Numerical time series of water free surface elevation (in red) and landslide thickness (in gray) measured at the eight gauges placed in the 3D domain (WG1, WG2, WG3, WG4, WG5, WG*, WG6, and WG7).

5.2. 2D Results (Far-Field)

In this section the results of the 2D model, fed by the 3D results at the interface boundary, are analyzed. Specifically, they are compared with two sets of observed data: the runup survey at the "out" location (see Figure 6) and the measured water level at the Yakutat tide station.

As stated, the interface boundary is located at the fjord section corresponding to the position of WG7. The free surface elevation time series, obtained by the 3D model at WG7, has been transformed by means of Fourier transform into the complex valued free-surface elevation $N^I(x, y; \omega_i)$, which was applied as wavemaker condition along the entire boundary (fjord section 1.8 km wide). The fluid velocity obtained by the 3D model has not been used as input for the 2D model. The rationale behind this configuration will be further discussed in the next section, where a sensitivity analysis of the 3D-2D coupling distance is carried out.

Figure 15 shows the free surface elevation time series at the three gauges (WG7, WG8, and WG9) placed within the 2D domain, as indicated in Figure 6. The black lines refer to the 2D model, while the input signal from the 3D model at WG7 is shown in red. The imperfect agreement between the 3D and 2D signals at WG7 is due to the smaller number of frequencies considered in the 2D simulation, which has an effect similar to a low-pass filter. The wave amplitude reaches approximately 15 m at WG7, and decreases to about 8 and 2 m respectively at WG8 and WG9. A similar trend is observed also for the wave troughs. This significant reduction in the wave height is due to the effect of the wave diffraction. Specifically, at gauge WG8 the wave front propagates through an area that is almost two times larger than that at WG7. Between WG8 and WG9 the waves has split in at least two components, one propagating toward the entrance of the large fjord (i.e., south-east) and one propagating up to the inner areas (north-west). The wave period remains almost constant at these three positions, that is, around 500 s (approximately 8 min).

After the discussion of the free surface elevation results, the analysis of the runup at the "out" location is now presented. As stated, for this analysis the numerical maximum runup values have been estimated using the semi-

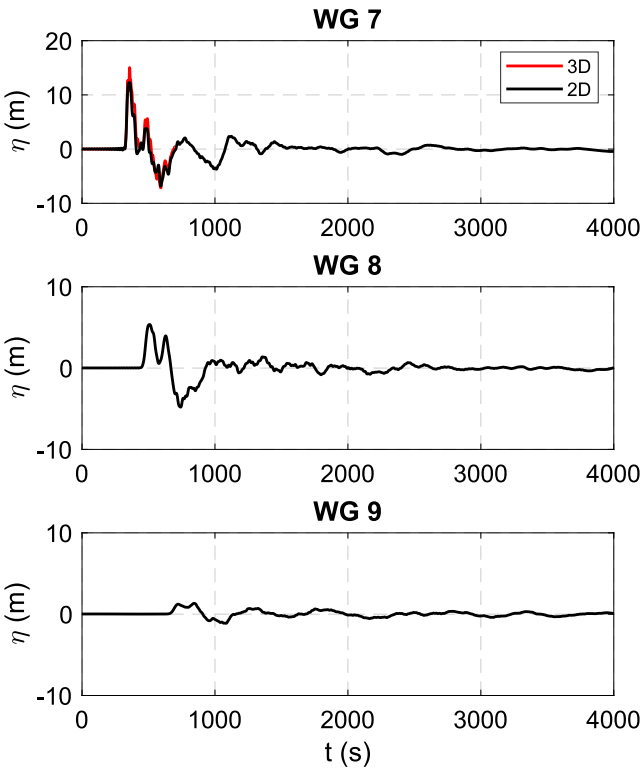

Figure 15. Numerical time series of water free surface elevation measured at the three gauges in the 2D domain (WG7, WG8, and WG9). Boundary interface placed in correspondence of WG7. Note: black lines refer to the 2D model results, while red lines to the 3D model ones.

empirical formula of Madsen and Fuhrman (2008) (Equation 8), which allows a comparison between survey and numerical data. The runup comparison is presented in Figure 16. In the left panel the runup (x-axis) is plotted against the latitude (y-axis). Survey data are reported using red filled circles, while the empty black circles represent the runup calculated with Equation 8, using as input the wave characteristics obtained by 2D model at the 41 extraction points located along the 50 m isobath. In the right panel, iso-water depth lines are shown, while the gray area represents the land. The locations at which the runup was measured in the field are reported using red circles, while the black empty circles show the position of the 41 save points. The black line represents the coastline.

The numerical results are comparable with the survey data. However, at some positions, quite large differences are observed between the two data sets. In general, the runup calculated on the basis of the numerical results is of the order of 5 m and no large variations are observed along the considered coastal stretch. This is probably due to the fact that the runup formula does not account for specific topo-bathymetric features that might have the effect of locally enhancing the inundation. On the contrary, at some positions in the central area of the stretch, the measured runup is much larger. It should also be noted that the Equation 8 uses an average sea bottom slope and does not take into account the slope of the inundated area, which on the contrary might have a very important effect when very different from $\overline{\alpha}$.

Finally, to assess the ability of the 3D-2D coupling approach to simulate the tsunami propagation in the very far-field, a quantitative comparison with the small tsunamis signal recorded at the Yakutat tide station is presented. Figure 17 shows the comparison between the free surface elevation time series obtained by the 2D simulation (black line) and that measured at the tidal station of Yakutat (gray line). The upper panel shows the comparison of the time series, while the lower one shows the frequency spectra. As described in the Section 3.3, the measured tsunami signal has been obtained by filtering out the astronomical tides. The numerical results were also down-sampled to one data point every 6 min, to ensure consistency with the measured signal sampling rate.

The comparison reveals an overall good agreement for both wave amplitudes and periods. The tsunami wave arrival time is coherent with the observations and the first two crests and troughs are well reproduced in shape. The frequency spectrum of the numerical signal shows a relevant amplification at $0.36 \cdot 10^{-3}$ Hz, which corresponds to the Helmholtz-type mode of resonance of Monti Bay. The measured time series shows, instead, a large energy peak at the frequency of the first longitudinal mode of the Yakutat Bay. It is not reproduced in the modeled tsunami signal, suggesting that this long wave component is forced by other metocean sources.

It is worth noting that simulating both the runup at the "out" location and, more importantly, the propagation of the tsunamis up to Yakutat Bay (distance between landslide impact point and tide station roughly 160 km) would be prohibitive with the 3D model, due to the size and shape of the domain that would lead to high computational times. The adopted 3D-2D coupling approach offers a practical and computationally efficient alternative for capturing both near- and far-field tsunami dynamics.

5.3. Sensitivity Analysis of the Coupling Distance

The previous section presented the 2D model results for the case with the interface boundary between 3D and 2D models located in correspondence of the position of the WG7. Nevertheless, the choice of the position of this boundary is a crucial point for the coupling technique. Indeed, on the one hand, the coupling interface should be set to minimize the 3D domain and therefore its computational times; on the other hand the extent of the 3D domain should be as large as possible to both provide a complete description of the near-field (where the local effects and nonlinear phenomena are important) and to provide an input for the 2D that is as accurate as possible. As previously mentioned, this coupling boundary should be ideally placed at the interface between the so-called near- and far-field. Nevertheless, it is commonly recognized by the scientific literature that the definition of the

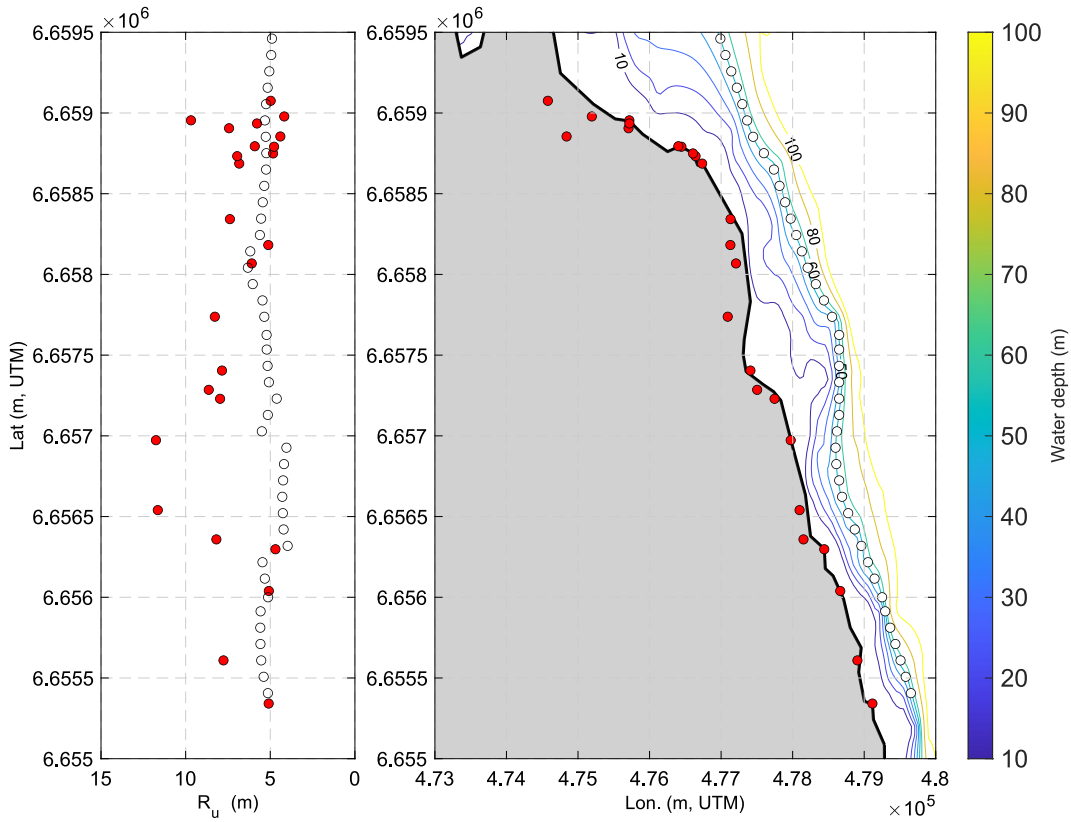

Figure 16. The runup comparison is presented in this figure. In the left panel the runup (x-axis) is plotted against the latitude (y-axis). Survey data are reported using red filled circles, while the empty black circles represent the runup calculated with Equation 8, using as input the wave characteristics obtained by 2D model at the 41 extraction points located along the 50 m isobath. In the right panel, iso-water depth lines are shown, while the gray area represents the land. The locations at which the runup was measured in the field are reported using red circles, while the black empty circles show the position of the 41 save points. The black line represents the coastline.

so-called near-field is ambiguous and, probably, strongly depends on local factors (e.g., topobathymetry characteristics).

To further investigate this crucial aspect, a sensitivity analysis of the position of the 3D-2D coupling interface is presented. In addition to the case presented in the previous section (where the interface boundary is located at the

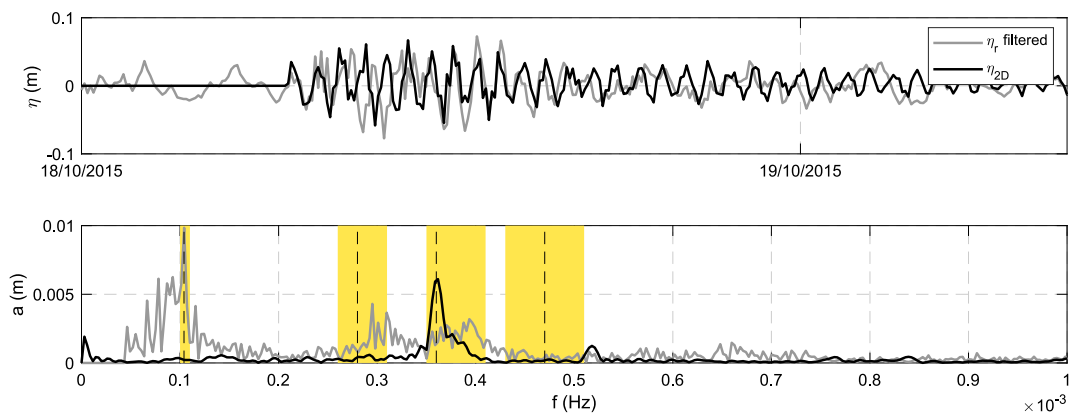

Figure 17. Comparison between the water level signal obtained by the 2D simulation (black line) and that measured at the tide station of Yakutat (gray line); in time (upper panel) and frequency (lower panels) domains.

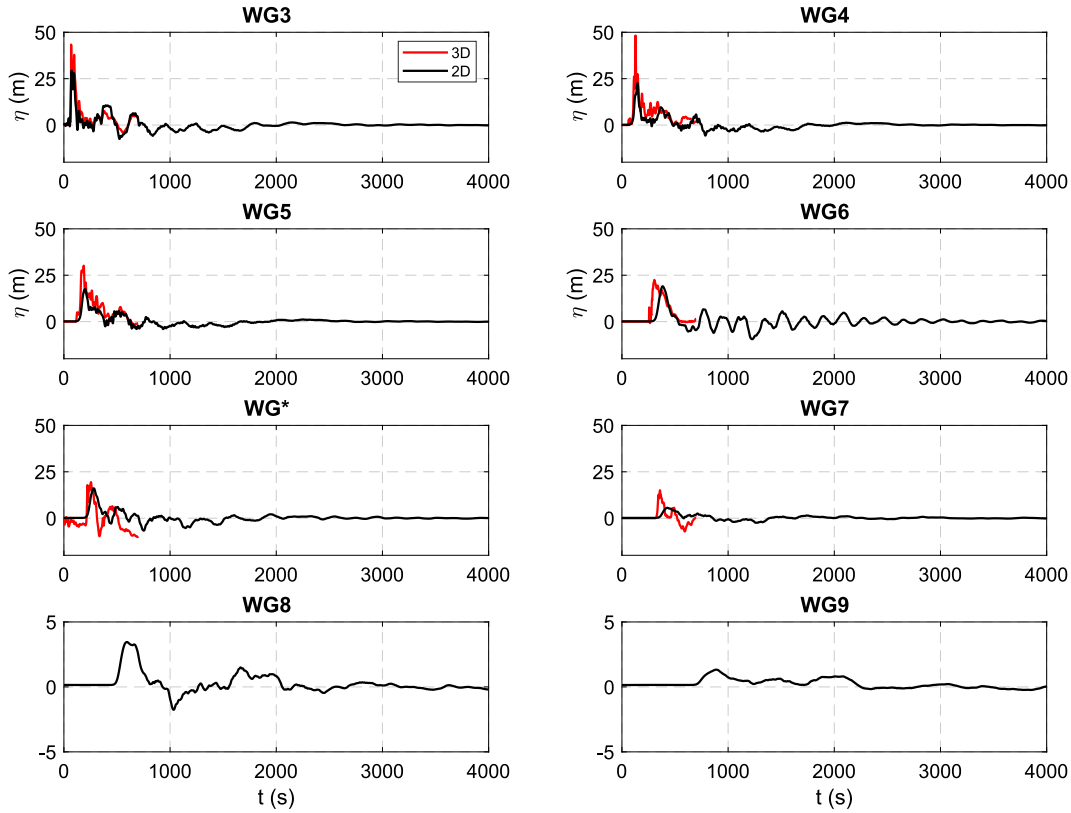

Figure 18. Numerical time series of water free surface elevation measured at eight gauges (WG3, WG4, WG5, WG6, WG*, WG7, WG8, and WG9). Boundary interface placed in the fjord section in correspondence of the WG3 position. Note: black lines refer to the 2D model results, while red lines to the 3D model ones.

position of WG7), two further simulations are examined, with the interface boundary at the position of WG3 and WG* (positions are shown in Figure 6). These three positions of the interface boundary represent "limit" conditions of the coupling strategy in the context of Taan Fiord tsunami event: (I) WG7, located very far from the landslide impact point and downstream of the bottleneck; (II) WG3, located very close to the landslide impact point and upstream of the bottleneck; (III) WG*, located at an intermediate distance and in correspondence of the bottleneck. While these positions and the related discussion are strictly related to the Taan Fiord case, this sensitivity analysis could be very useful to provide some general insights when designing a 3D-2D coupling strategy for landslide-generated tsunamis in complex geometries. In fact, the discussion related to the following results can guide the selection of the 3D-2D coupling distance considering the local topobathmetry, the degree of confinement and the hydrodynamic characteristics of the case at hand.

Thus, the 2D model has been applied in three different 2D numerical domains, which differ regarding the position of the wavemaker boundary, WG3, WG*, and WG7 (the latter previously discussed). The effectiveness of each coupling configurations has been evaluated by comparing the 2D model free surface elevations and runup with the 3D free surface elevation results (where available) and the runup survey data at the "out" location, respectively.

Figure 18 shows the numerical results obtained when the 2D model is forced with the 3D model results extracted at WG3. The numerical time series of water free surface elevation are represented with black and red lines for the 2D and 3D models, respectively. It should be noted that the mismatch between 3D and 2D signals at WG3 is related to the reduced number of frequencies considered in the 2D simulations. This aspect, also noticeable when imposing the interface boundary between 3D and 2D at WG7 (and WG*), is more evident at WG3. In fact, this gauge is located very close to the landslide impact point (near-field) and consequently, the tsunami is characterized by shorter wave periods. The comparison indicates that the 2D model provides a reasonable, albeit underestimated, reproduction of the tsunami waveform upstream of the bottleneck (WG4 and WG5) and in correspondence of the bottleneck (WG* and WG6). On the contrary, downstream of the bottleneck (see WG7),

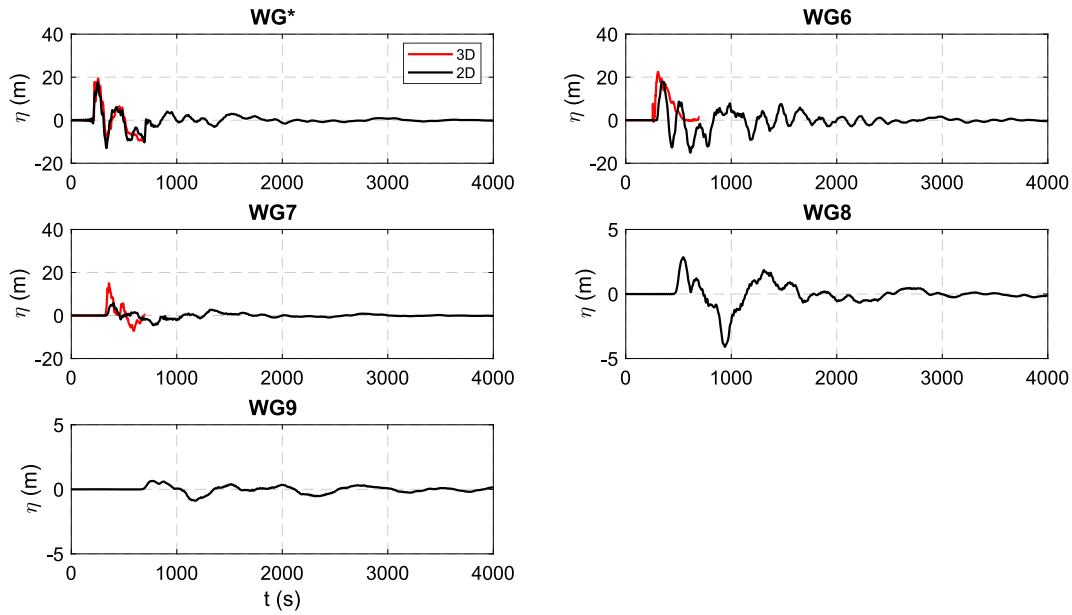

Figure 19. Numerical time series of water free surface elevation measured at eight gauges (WG*, WG6, WG7, WG8, and WG9). Boundary interface placed in the fjord section in correspondence of the WG* position. Note: black lines refer to the 2D model results, while red lines to the 3D model ones.

the 2D signal is significantly different from the 3D one. This is clearly due to the inability of the 2D model to simulate the lateral expansion and inundation at the shallow waters area between WG* and WG7, while this is well modeled by the 3D model (see Figure 10).

A similar pattern is observed in Figure 19, which shows the results when the 2D model is fed at WG*, that is, at the bottleneck. For this configuration, although 2D results at WG6 are comparable in term of wave amplitude with those obtained by the 3D model, again the free surface elevation time series downstream of the bottleneck (see WG7) is not well reproduced.

Finally, in order to further compare the performance of the 2D model when fed at these three positions of the interface boundary, the comparison with the survey runup data at the "out" location is presented in Figure 20. The

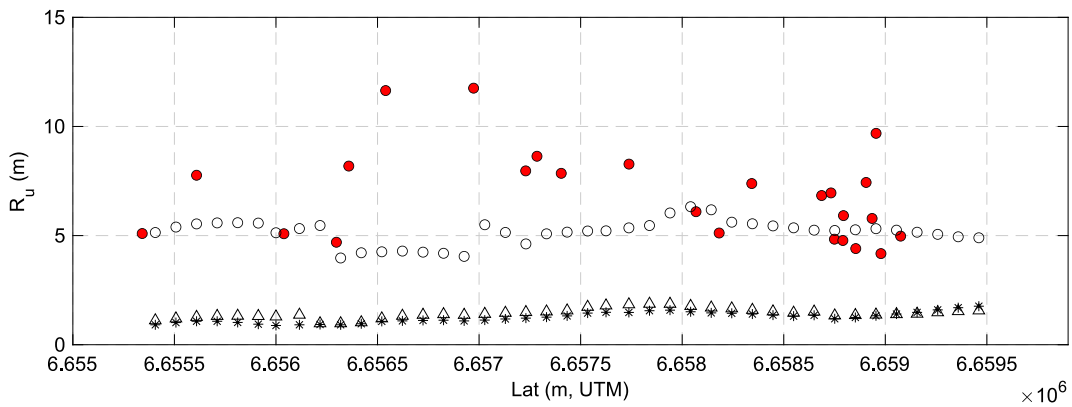

Figure 20. Results of the sensitivity analysis in term of runup at "out" location: comparison between survey runup (full red circles) and runup calculated with Equation 8, using as input the wave characteristics obtained by 2D model at the 41 extraction points located along the 50 m isobath. Refer to the right panel of Figure 16 for the 41 extraction points locations. Note: empty black circles are the numerical runup coupling 3D and 2D models at section where WG7 is located; black asterisks and triangles are the numerical runup coupling 3D and 2D models at sections where WG3 and WG* are located, respectively.

organization of this figure is similar to the left panel of Figure 16. Red circles represent runup survey values, while black markers represent the runup calculated with Equation 8. Specifically, black circles, triangles, and asterisks represent the runup values calculated starting from the 2D model results fed by the 3D model at WG7, WG*, and WG3, respectively.

To summarize, this comparison confirms the earlier findings based on the free surface elevation analysis. When the 2D model is fed with the 3D results extracted upstream of the bottleneck, the model provides poor estimate of the runup and of the tsunamis signal in general. In fact, in this part of the domain the 3D effects, which take place both in the very near-field (i.e., generation area) and during the propagation (e.g., due to local topobathmetry and/or degree of confinement), are dominant. On the contrary, if the coupling takes place downstream of the bottleneck, the runup pattern, although if estimated with a simplified tool, exhibits an overall good agreement with the survey data. Thus, although these considerations are specific to the case at hand, they can offer general insights for designing a 3D-2D coupling strategy for landslide-generated tsunamis in complex geometries.

5.4. Limitations

In this section, some of the limitations of the present study are discussed. The first is related to the significant uncertainty that affects the estimate of the volume and shape of the landslide. Another limitation is related to the landslide modeling which, in the 3D model, is represented as an homogeneous granular material governed by a simple rheological model, while in reality it is made by a heterogeneous medium. This is clearly a simplification, as for the used rheological model the landslide material is globally described with few physical parameters. Furthermore, the present numerical method is based on a multiphase approach, in which mixing and permeation among phases are not properly modeled. The lack of water permeation into the granular material may result in larger wave characteristics (Lindstrøm, 2016).

Regarding the 2D model, it should be noted that it is based on a set of linearized equations and is therefore not capable of reproducing the nonlinear phenomena that often dominate tsunami dynamics in the near-field, as shown in the previous section. For this reason, the appropriate selection of the coupling distance is crucial. In this line, the 2D model has fixed boundaries, thus it cannot properly reproduce coastal flooding. Therefore, the semi-empirical formula of Madsen and Fuhrman (2008) has been used for estimating the runup in the far-field, which is only suitable for incident waves orthogonal to the shoreline and constant coastal slope.

Another limitation is related to the very far-field tsunamis measurements at Yakutat used for comparison. The tsunami signal, measured by the tides station, is very small, with wave heights of the order of few centimeters. It is in general difficult to deal with small quantities, as measurement errors and other sources of long waves might obscure the data of interest.

6. Conclusions

In this paper, a coupling strategy between 3D and 2D models for simulating landslide-generated tsunamis in complex geometries has been presented. The objective of this modeling strategy is to maximize the accuracy of near-field simulations while minimizing computational costs, thereby enabling efficient long-range wave propagation. To this end, the model chain is made of two models, namely: a 3D model, OpenFOAM® (Romano et al., 2023), used for simulating the landslide-tsunamis characteristics in the near-field and a 2D model based on the MSE (Cecioni et al., 2023), fed by 3D results and used for efficiently propagating the tsunamis in the far-field.

The proposed coupling strategy has been applied to reproduce numerically the 2015 Taan Fiord (AK) landslide-tsunami event. This event has been selected due to several reasons. First, it is very well-documented, with extensive high-quality field data available to support the modeling and enable validation. Specifically, high-resolution pre- and post-event topobathymetric surveys and runup measurements (Haeussler et al., 2018; Higman et al., 2018; Lynett et al., 2025), along with tidal gauge data from the Yakutat station, located approximately 160 km away, provide valuable observational constraints. Second, it serves as a representative example of "complex geometry." In fact, it presents near-field challenges due to the confined fjord environment, which necessitate the use of sophisticated numerical models (3D, 2D multi-layer, etc.) to accurately capture the tsunamis dynamics. At the same time, the area of interest for the far-field simulation is large, thus the use of a more computationally efficient 2D model is highly recommended. Moreover, the tide gauge, used to evaluate the capability of the coupling strategy in simulating the tsunamis characteristics in the very far-field, is located within

a small bay, thus a detailed analysis to isolate the tsunami signal from other coexisting physical phenomena has been carried out taking advantage of the capabilities of the 2D model. Lastly, this case has been included as one of the benchmarks of a recent workshop on subaerial landslide-generated tsunamis intercomparison study, organized by Prof. Patrick Lynett (University of Southern California) and Dr. Katherine Barnhart (United States Geological Survey, USGS) in February 2025 in Golden, Colorado (USA), in which the authors participated.

Thus, the 2015 Taan Fiord event has been numerically reproduced, and the accuracy of the proposed coupling methodology was assessed through comparison with field data. Overall, it can be stated that the 3D-2D coupling strategy provided results which are in overall good agreement with surveys, both in the near- and the far-field. As far as the near-field is concerned, the tsunamis generation, propagation and runup phenomena are generally well caught by the 3D model, especially considering the factors that are expected to control this complex process. In fact, despite the articulated topobathymetry, the high degree of confinement, the nonlinear effects, and the relevant sources of uncertainty that characterize the definition of the landslide scenario, the numerical data well reproduce the survey runup pattern ("near" and "mid" locations) and flow elevations.

Also the 2D model, fed by the 3D results, provides results which are comparable with the survey data. The runup estimated at the "out" location, although calculated with a semi-empirical formula (Madsen & Fuhrman, 2008), whose applicability to the case under consideration is not perfect, show an overall good agreement with the survey data. In the very far-field, the comparison between the numerical free surface elevation time series and the small tsunamis signal measured at the Yakutat tide station shows that the model chain is able to reproduce the tsunamis properties, in terms of both wave characteristics (wave amplitudes and periods) and tsunami wave arrival time. It is worth noticing that, while the 2D model is not suitable for capturing nonlinear features or simulating inundation processes, as acknowledged in the limitations of this study (Section 5.4), its use serves a dual purpose: propagating tsunami waveforms in the very far-field at low computational cost and analyzing resonant natural modes for configuration such as bays, fjords, small volcanic islands, etc. The latter point is particularly critical for interpreting sea level measurements of small tsunami signals, especially when recorded by stations located in complex coastal configurations.

In fact, a careful analysis of the tidal signal measured at Yakutat has been carried out. First, on the basis of the harmonic tidal analysis, the astronomical tide signal has been removed from the data. Then, the residual has been found to have a frequency spectrum that shows large energy at some frequency bands. This has suggested that both the tsunami and possible other meteorological disturbances have excited some eigenmodes of the bay, where the gauge is located. In order to investigate this mechanism, a resonance analysis has been performed using the 2D MSE model. The analysis has confirmed that some Monti and Yakutat bays eigenmodes are excited by the tsunami, influencing the amplitude and the period of the waves measured by the instrument.

Finally, although the results and the related discussions presented in this work are strictly related to the Taan Fiord case, the methodology presented could offer some general insights and practical guidance for the application of this modeling chain to landslide-tsunami events in complex geometries. To this end, a sensitivity analysis, by varying the position of the coupling boundary between the two models, has been performed. This analysis demonstrated that delimiting the near-field is challenging, as it strongly depends on local conditions, such as the landslide characteristics, topobathymetry, degree of confinement, etc. Nevertheless, useful insights emerged from the analysis. Specifically, the analysis allows to hypothesize, at least for the considered case, that in the absence of topobathymetric singularities (e.g., the fjord's bottleneck), the coupling distance can be positioned very close to the impact point, thereby reducing computational cost while maintaining modeling accuracy. Conversely, when such singularities are present, they should be included within the 3D domain (ideally positioned far from the interface boundary between the two numerical domains) to avoid inaccuracies in far-field modeling.

Conflict of Interest

The authors declare no conflicts of interest relevant to this study.

Data Availability Statement

The data set presented in this research are provided as Supporting Information.

Acknowledgments
Prof. Patrick Lynett (University of Southern California) and Dr. Katherine Barnhart (United States Geological Survey, USGS) are sincerely acknowledged for organizing the workshop on subaerial landslide intercomparison benchmark study in February 2025 in Golden, Colorado (USA). Dr. Paula Núñez (IHCantabria) is warmly acknowledged for the fruitful discussion on the tidal analysis.

References

Abadie, S., Morichon, D., Grilli, S., & Glockner, S. (2010). Numerical simulation of waves generated by landslides using a multiple-fluid Navier–Stokes model. *Coastal Engineering*, *57*(9), 779–794. https://doi.org/10.1016/j.coastaleng.2010.03.003

Abadie, S., Parvin, A. H., El Omari, K., Le Guer, Y., Louis-Napoléon, A., & Rozki, M. (2025). On the optimum of the energy transfer efficiency in the generation of waves by subaerial landslides. *Communications Earth & Environment*, *6*(1), 729. https://doi.org/10.1038/s43247-025-02740-0

Aranguiz, R., Catalán, P., Cecioni, C., Bellotti, G., Henriquez, P., & González, J. (2019). Tsunami resonance and spatial pattern of natural oscillation modes with multiple resonators. *Journal of Geophysical Research: Oceans*, *124*(11), 7797–7816. https://doi.org/10.1029/2019jc015206

Bellotti, G., Briganti, R., & Beltrami, G. (2012). The combined role of Bay and shelf modes in tsunami amplification along the coast. *Journal of Geophysical Research*, *117*(8), 555. https://doi.org/10.1029/2012jc008061

Bellotti, G., Cecioni, C., & De Girolamo, P. (2008). Simulation of small-amplitude frequency-dispersive transient waves by means of the mild-slope equation. *Coastal Engineering*, *55*(6), 447–458. https://doi.org/10.1016/j.coastaleng.2007.12.006

Bellotti, G., & Romano, A. (2017). Wavenumber-frequency analysis of landslide-generated tsunamis at a conical island. Part II: EOF and modal analysis. *Coastal Engineering*, *128*, 84–91. https://doi.org/10.1016/j.coastaleng.2017.07.008

Bloom, C., MacInnes, B., Higman, B., Shugar, D., Venditti, J., Richmond, B., & Bilderback, E. (2020). Catastrophic landscape modification from a massive landslide tsunami in Taan Fiord, Alaska. *Geomorphology*, *353*, 107029. https://doi.org/10.1016/j.geomorph.2019.107029

Brackbill, J. U., Kothe, D. B., & Zemach, C. (1992). A continuum method for modeling surface tension. *Journal of Computational Physics*, *100*(2), 335–354. https://doi.org/10.1016/0021-9991(92)90240-y

Bullard, G., Mulligan, R., Carreira, A., & Take, W. (2019). Experimental analysis of tsunamis generated by the impact of landslides with high mobility. *Coastal Engineering*, *152*, 103538. https://doi.org/10.1016/j.coastaleng.2019.103538

Cecioni, C., & Bellotti, G. (2010a). Modeling tsunamis generated by submerged landslides using depth integrated equations. *Applied Ocean Research*, *32*(3), 343–350. https://doi.org/10.1016/j.apor.2009.12.002

Cecioni, C., & Bellotti, G. (2010b). Inclusion of landslide tsunamis generation into a depth integrated wave model. *Natural Hazards and Earth System Sciences*, *10*(11), 2259–2268. https://doi.org/10.5194/nhess-10-2259-2010

Cecioni, C., Iorio, V., Bellotti, G., & Grilli, S. T. (2023). Probabilistic landslide tsunami modeling of the 2018 Palu Bay event. *Coastal Engineering*, *183*, 104332. https://doi.org/10.1016/j.coastaleng.2023.104332

Cecioni, C., Romano, A., Bellotti, G., Di Risio, M., & De Girolamo, P. (2011). Real-time inversion of tsunamis generated by landslides. *Natural Hazards and Earth System Sciences*, *11*(9), 2511–2520. https://doi.org/10.5194/nhess-11-2511-2011

Corsa, B., Jacquemart, M., Willis, M., & Tiampo, K. (2022). Characterization of large tsunamigenic landslides and their effects using digital surface models: A case study from Taan Fiord, Alaska. *Remote Sensing of Environment*, *270*, 112881. https://doi.org/10.1016/j.rse.2021.112881

Cortés, P., Catalán, P. A., Aránguiz, R., & Bellotti, G. (2017). Tsunami and shelf resonance on the northern Chile coast. *Journal of Geophysical Research: Oceans*, *122*(9), 7364–7379. https://doi.org/10.1002/2017jc012922

Di Risio, M., Bellotti, G., Panizzo, A., & De Girolamo, P. (2009). Three-dimensional experiments on landslide generated waves at a sloping coast. *Coastal Engineering*, *56*(5–6), 659–671. https://doi.org/10.1016/j.coastaleng.2009.01.009

Di Risio, M., De Girolamo, P., Bellotti, G., Panizzo, A., Aristodemo, F., Molfetta, M. G., & Petrillo, A. F. (2009). Landslide-generated tsunamis runup at the coast of a conical island: New physical model experiments. *Journal of Geophysical Research*, *114*(C1), C01009. https://doi.org/10.1029/2008jc004858

Domnik, B., & Pudasaini, S. P. (2012). Full two-dimensional rapid chute flows of simple viscoplastic granular materials with a pressure-dependent dynamic slip-velocity and their numerical simulations. *Journal of Non-Newtonian Fluid Mechanics*, *173*, 72–86. https://doi.org/10.1016/j.jnnfm.2012.03.001

Enet, F., & Grilli, S. T. (2007). Experimental study of tsunami generation by three-dimensional rigid underwater landslides. *Journal of Waterway Port Coastal and Ocean Engineering-ASCE*, *133*(6), 442–454. https://doi.org/10.1061/(asce)0733-950x(2007)133:6(442)

Franco, A., Moernaut, J., Schneider-Muntau, B., Strasser, M., & Gems, B. (2021). Triggers and consequences of landslide-induced impulse waves–3D dynamic reconstruction of the Taan Fiord 2015 tsunami event. *Engineering Geology*, *294*, 106384. https://doi.org/10.1016/j.enggeo.2021.106384

Fritz, H. M., Mohammed, F., & Yoo, J. (2009). Lituya Bay landslide impact generated mega-tsunami 50th anniversary. *Pure and Applied Geophysics*, *166*(1–2), 153–175. https://doi.org/10.1007/s00024-008-0435-4

Grilli, S. T., Shelby, M., Kimmoun, O., Dupont, G., Nicolsky, D., Ma, G., et al. (2017). Modeling coastal tsunami hazard from submarine mass failures: Effect of slide rheology, experimental validation, and case studies off the US east coast. *Natural Hazards*, *86*(1), 353–391. https://doi.org/10.1007/s11069-016-2692-3

Grilli, S. T., Tappin, D. R., Carey, S., Watt, S. F., Ward, S. N., Grilli, A. R., et al. (2019). Modelling of the tsunami from the December 22, 2018 lateral collapse of Anak Krakatau volcano in the Sunda Straits, Indonesia. *Scientific Reports*, *9*(1), 11946. https://doi.org/10.1038/s41598-019-48327-6

Grilli, S. T., Taylor, O.-D. S., Baxter, C. D., & Maretzki, S. (2009). A probabilistic approach for determining submarine landslide tsunami hazard along the upper east coast of the United States. *Marine Geology*, *264*(1–2), 74–97. https://doi.org/10.1016/j.margeo.2009.02.010

Haeussler, P. J., Gulick, S., McCall, N., Walton, M., Reece, R., Larsen, C., et al. (2018). Submarine deposition of a subaerial landslide in Taan Fiord, Alaska. *Journal of Geophysical Research: Earth Surface*, *123*(10), 2443–2463. https://doi.org/10.1029/2018jf004608

Heller, V., & Spinneken, J. (2013). Improved landslide-tsunami prediction: Effects of block model parameters and slide model. *Journal of Geophysical Research: Oceans*, *118*(3), 1489–1507. https://doi.org/10.1002/jgrc.20099

Heller, V., & Spinneken, J. (2015). On the effect of the water body geometry on landslide–Tsunamis: Physical insight from laboratory tests and 2D to 3D wave parameter transformation. *Coastal Engineering*, *104*, 113–134. https://doi.org/10.1016/j.coastaleng.2015.06.006

Higman, B., Shugar, D. H., Stark, C. P., Ekström, G., Koppes, M. N., Lynett, P., et al. (2018). The 2015 landslide and tsunami in Taan Fiord, Alaska. *Scientific Reports*, *8*(1), 12993. https://doi.org/10.1038/s41598-018-30475-w

Higuera, P., Lara, J. L., & Losada, I. J. (2013a). Realistic wave generation and active wave absorption for Navier–Stokes models: Application to OpenFOAM®. *Coastal Engineering*, *71*, 102–118. https://doi.org/10.1016/j.coastaleng.2012.07.002

Higuera, P., Lara, J. L., & Losada, I. J. (2013b). Simulating coastal engineering processes with OpenFOAM®. *Coastal Engineering*, *71*, 119–134. https://doi.org/10.1016/j.coastaleng.2012.06.002

Iorio, V., Bellotti, G., Cecioni, C., & Grilli, S. T. (2021). A numerical model for the efficient simulation of multiple landslide-induced tsunamis scenarios. *Ocean Modelling*, *168*, 101899. https://doi.org/10.1016/j.ocemod.2021.101899

Jasak, H. (1996). *Error analysis and estimation for the finite volume method with applications to fluid flows. (Ph.D thesis)*. Imperial College London (University of London).

Larsen, B. E., & Fuhrman, D. R. (2018). On the over-production of turbulence beneath surface waves in Reynolds-averaged Navier–Stokes models. *Journal of Fluid Mechanics*, *853*, 419–460. https://doi.org/10.1017/jfm.2018.577

Lindstrøm, E. K. (2016). Waves generated by subaerial slides with various porosities. *Coastal Engineering*, *116*, 170–179. https://doi.org/10.1016/j.coastaleng.2016.07.001

Løvholt, F., Glimsdal, S., & Harbitz, C. B. (2020). On the landslide tsunami uncertainty and hazard. *Landslides*, *17*(10), 2301–2315. https://doi.org/10.1007/s10346-020-01429-z

Lynett, P., & Liu, P. L. F. (2005). A numerical study of the run-up generated by three-dimensional landslides. *Journal of Geophysical Research*, *110*(C3), C03006. https://doi.org/10.1029/2004jc002443

Lynett, P., Weiss, R., Higman, B., Mattox, A., Keen, A., Skanavis, V., et al. (2025). Tsunami runup survey data from the Taan Fjord landslide event. *Scientific Data*, *12*(1), 1341. https://doi.org/10.1038/s41597-025-05617-1

Madsen, P., & Fuhrman, D. (2008). Run-up of tsunamis and long waves in terms of surf-similarity. *Coastal Engineering*, *55*(3), 209–223. https://doi.org/10.1016/j.coastaleng.2007.09.007

Marschall, H., Hinterberger, K., Schüler, C., Habla, F., & Hinrichsen, O. (2012). Numerical simulation of species transfer across fluid interfaces in free-surface flows using OpenFOAM. *Chemical Engineering Science*, *78*, 111–127. https://doi.org/10.1016/j.ces.2012.02.034

McFall, B. C., & Fritz, H. M. (2016). Physical modelling of tsunamis generated by three-dimensional deformable granular landslides on planar and conical island slopes. *Proceedings of the Royal Society of London. Series A: Mathematical, Physical and Engineering Sciences*, *472–2188*(2188), 20160052. https://doi.org/10.1098/rspa.2016.0052

Miller, G. S., Take, W. A., Mulligan, R. P., & McDougall, S. (2017). Tsunamis generated by long and thin granular landslides in a large flume. *Journal of Geophysical Research: Oceans*, *122*(1), 653–668. https://doi.org/10.1002/2016jc012177

Mohammed, F., & Fritz, H. M. (2012). Physical modeling of tsunamis generated by three-dimensional deformable granular landslides. *Journal of Geophysical Research*, *117*(C11). https://doi.org/10.1029/2011jc007850

Mulligan, R. P., & Take, W. A. (2017). On the transfer of momentum from a granular landslide to a water wave. *Coastal Engineering*, *125*, 16–22. https://doi.org/10.1016/j.coastaleng.2017.04.001

Mulligan, R. P., Franci, A., Celigueta, M. A., & Take, W. A. (2020). Simulations of landslide wave generation and propagation using the particle finite element method. *Journal of Geophysical Research: Oceans*, *125*(6), e2019JC015873. https://doi.org/10.1029/2019JC015873

Paris, A., Heinrich, P., & Abadie, S. (2021). Landslide tsunamis: Comparison between depth-averaged and Navier–Stokes models. *Coastal Engineering*, *170*, 104022. https://doi.org/10.1016/j.coastaleng.2021.104022

Rauter, M., Hoße, L., Mulligan, R., Take, W., & Løvholt, F. (2021). Numerical simulation of impulse wave generation by idealized landslides with OpenFOAM. *Coastal Engineering*, *165*, 103815. https://doi.org/10.1016/j.coastaleng.2020.103815

Rauter, M., Viroulet, S., Gylfadóttir, S. S., Fellin, W., & Løvholt, F. (2022). Granular porous landslide tsunami modelling–the 2014 Lake Askja flank collapse. *Nature Communications*, *13*(1), 1–13. https://doi.org/10.1038/s41467-022-28296-7

Romano, A., Bellotti, G., Barajas, G., & Lara, J. L. (2025). On the energy transfer of tsunamis generated by subaerial granular landslides: A 2D numerical analysis. *Coastal Engineering*, *202*, 104821. https://doi.org/10.1016/j.coastaleng.2025.104821

Romano, A., Bellotti, G., & Di Risio, M. (2013). Wavenumber–frequency analysis of the landslide-generated tsunamis at a conical island. *Coastal Engineering*, *81*, 32–43. https://doi.org/10.1016/j.coastaleng.2013.06.007

Romano, A., Di Risio, M., Bellotti, G., Molfetta, M., Damiani, L., & De Girolamo, P. (2016). Tsunamis generated by landslides at the coast of conical islands: Experimental benchmark dataset for mathematical model validation. *Landslides*, *13*(6), 1379–1393. https://doi.org/10.1007/s10346-016-0696-4

Romano, A., Lara, J. L., Barajas, G., Di Paolo, B., Bellotti, G., Di Risio, M., et al. (2020). Tsunamis generated by submerged landslides: Numerical analysis of the near-field wave characteristics. *Journal of Geophysical Research: Oceans*, *125*(7), e2020JC016157. https://doi.org/10.1029/2020jc016157

Romano, A., Lara, J. L., Barajas, G., & Losada, Í. J. (2023). Numerical modeling of tsunamis generated by granular landslides in OpenFOAM®: A Coulomb viscoplastic rheology. *Coastal Engineering*, *186*, 104391. https://doi.org/10.1016/j.coastaleng.2023.104391

Sammarco, P., Fischione, P., Romano, A., Bellotti, G., & Dalla Villa, S. (2024). Prototype data analysis of the dynamics of the Venice gate-barriers during an extreme storm event. *Coastal Engineering*, *194*, 104623. https://doi.org/10.1016/j.coastaleng.2024.104623

von Boetticher, A., Turowski, J. M., McArdell, B. W., Rickenmann, D., & Kirchner, J. W. (2016). Debrisintermixing-2.3: A finite volume solver for three-dimensional debris-flow simulations with two calibration parameters—Part 1: Model description. *Geoscientific Model Development*, *9*(9), 2909–2923. https://doi.org/10.5194/gmd-9-2909-2016

Weller, H. G. (2008). *A new approach to VOF-based interface capturing methods for incompressible and compressible flow, Report TR/HGW, 4*. OpenCFD Ltd.